Available online at www.sciencedirect.com

ScienceDirect

International Journal of Solids and Structures 43 (2006) 7197–7222

INTERNATIONAL JOURNAL OF SOLIDS and STRUCTURES

www.elsevier.com/locate/ijsolstr

A phenomenological constitutive model for ferroelastic and ferroelectric hysteresis effects in ferroelectric ceramics

S. Klinkel *

Institut für Baustatik, Universität Karlsruhe, Kaiserstr. 12, 76131 Karlsruhe, Germany

Received 4 January 2006; received in revised form 28 February 2006
Available online 20 March 2006

Abstract

This paper is concerned with a macroscopic constitutive law for domain switching effects, which occur in ferroelectric ceramics. The three-dimensional model is thermodynamically consistent and is determined by two scalar valued functions: the Helmholtz free energy and a switching surface. In a kinematic hardening process the movement of the center of the switching surface is controlled by internal variables. In common usage, the remanent polarization and the irreversible strain are employed as internal variables. The novel aspect of the present work is to introduce an irreversible electric field, which serves instead of the remanent polarization as internal variable. The irreversible electric field has only theoretical meaning, but it makes the formulation very suitable for a finite element implementation, where displacements and the electric potential are the nodal degrees of freedom. The paper presents an appropriate implementation into a hexahedral finite brick element. The uni-axial constitutive model successfully reproduces the ferroelastic and the ferroelectric hysteresis as well as the butterfly hysteresis for ferroelectric ceramics. Furthermore it accounts for the mechanical depolarization effect, which occurs if the polarized ferroelectric ceramic is subjected to a compression stress.

Keywords: Constitutive law; Ferroelastic; Ferroelectric; Hysteresis; Piezoelectric ceramic; Finite element method; Smart materials

1. Introduction

Piezoelectric devices are found in a wide range of applications, for a detailed discussion see Tani et al. (1998), Niezrecki et al. (2001) and Jendritza (2005). The variety of applications include also micro electro mechanical systems, see e.g. Maluf and Williams (2004). A reliability analysis necessitates a calculation of the stress state in piezoelectric ceramics as precisely as possible. This motivates the present work to deal with the constitutive law. A phenomenological fully coupled macroscopic constitutive relation including hysteresis effects and its consistent finite element implementation is proposed.

In this paper it is distinguished between a piezoelectric ceramic and ferroelectric ceramic, where a piezoelectric ceramic is defined as a poled ferroelectric material. Typical materials for the utilization of the piezoelectric

* Tel.: +49 721 608 2280; fax: +49 721 608 6015.
E-mail address: sk@bs.uni-karlsruhe.de

0020-7683/$ - see front matter © 2006 Published by Elsevier Ltd.
doi:10.1016/j.ijsolstr.2006.03.008

effect are barium titanate ($BaTiO_3$) and lead zirconate titanate ($PbZrTiO_3$) abbreviated as PZT, see e.g. Moulson and Herbert (2003). The material nonlinear behavior occurs due to switching effects of the single crystals, where atoms change from one possible position to another. Microscopically motivated material models are presented by e.g. Chen and Lynch (1998), Hwang et al. (1998), Huber et al. (1999) and Huber and Fleck (2001). These models are concerned with the constitutive behavior of single crystals and employ an energy argument as switching criterion. The over all material behavior of a ceramic polycrystal is obtained by averaging over a large number of oriented crystallites. The consideration of switching for each crystal leads to a large number of internal variables.

The reduction of the number of internal variables motivates phenomenological macroscopical models. A very simple model to capture arbitrary hysteresis effects is the so-called Preisach-model, introduced in Preisach (1935). The model needs only a few material parameters and was originally developed to describe effects arising in magnetization processes. In recent years the model is successfully adopted to model ferroelectric ceramics, see e.g. Hwang et al. (1995), Simkovics et al. (2000), Pasco and Berry (2004), Yu et al. (2002) and Butz et al. (2005). Hwang et al. (1995) employed the Preisach model to predict the remanent polarization and the remanent strain from an imposed electric field and a stress. They introduced a simple fully coupled one-dimensional model with uni-axial loading. In Simkovics et al. (2000), Yu et al. (2002) and Pasco and Berry (2004) the Preisach model is utilized to account only for the dielectric hysteresis. With this model Simkovics et al. (2000) are able to simulate higher order harmonics produced by piezoelectric transducers correctly. The work of Pasco and Berry (2004) focuses on minor loops around the initial state of polarization. In Butz et al. (2005) the Preisach approach is implemented in a three-dimensional beam finite element to model the dielectric and the butterfly hysteresis.

Another approach for a phenomenological model based on a macroscopic theory is suggested in Chen and Montgomery (1980), Chen (1980) and Chen and Tucker (1981). The key idea is that the remanent polarization is a function of aligned dipoles. The number of the aligned dipoles is used as an internal state variable. The model is able to represent the uni-axial dielectric and the butterfly hysteresis. Similarly to Preisach the model is not thermodynamically motivated.

A thermodynamically sound phenomenological model is presented in Bassiouny et al. (1988a,b) and Bassiouny and Maugin (1989a,b). A free energy function per unit volume depending on temperature, strain and the polarization is introduced. The polarization is additively decomposed into a reversible and an irreversible part, which serves as internal state variable. According to thermodynamic arguments the constitutive relations are derived within the Clausius–Duhem inequality. For rate independent effects an electric loading function (switching criterion) is suggested to determine the evolution of the internal state variable.

On the basis of this concept several models for domain switching effects have been developed, see Cocks and McMeeking (1999), Kamlah and Tsakmakis (1999), Kamlah (2001), Kamlah and Böhle (2001), McMeeking and Landis (2002), Landis (2002), Schröder and Romanowski (2004, 2005) and Elhadrouz et al. (2004, 2005). In all these contributions the irreversible polarization and irreversible strains serve as internal variables to control the kinematic hardening process.

Cocks and McMeeking (1999) and Kamlah and Tsakmakis (1999) introduced uni-axial models. In Kamlah and Tsakmakis (1999) and Kamlah (2001) the irreversible strain is additively decomposed into two parts. One irreversible strain appears due to the alignment of the domains in a certain direction by applying an electrical loading. For this strain a one-to-one relationship to the irreversible polarization is assumed. The other irreversible strain arises due to mechanical stresses and is determined by an evolution equation. In Kamlah (2001) four switching criteria are described, which characterize the onset and the saturation of domain switching. A three dimensional extension of the model is presented in Kamlah and Böhle (2001). It is capable to simulate all hysteresis and butterfly loops including mechanical depolarization effects, which arise in ferroelectric ceramics. A model which makes use of only one switching criterium is suggested by Schröder and Romanowski (2004, 2005). The co-ordinate invariant thermodynamic consistent model is based on the work of Schröder and Gross (2004) and accounts for two hysteresis effects: the ferroelectric hysteresis and the butterfly hysteresis. In the uni-axial model the polarization direction is assumed to be constant. Furthermore the model makes use of the simplifying one-to-one relation discussed above. The uni-axial model of Elhadrouz et al. (2004, 2005) considers the additive split of the irreversible strains proposed by Kamlah and Tsakmakis (1999). For one part the discussed one-to-one relationship is assumed. Furthermore Elhadrouz et al. introduced an

additive decomposition of the irreversible depolarization, where it is distinguished between a polarization caused by an electric field and a polarization caused by stress. Two switching criteria are used to control the different ferroelastic and ferroelectric hysteresis and butterfly loops. The model is also able to predict mechanical depolarization.

Multi-axial constitutive laws are introduced in McMeeking and Landis (2002) and Landis (2002). Multi-axial models are necessary to fit the polarization rotation behavior of ferroelectric ceramics. In McMeeking and Landis (2002) the one-to-one relationship between the irreversible polarization and the irreversible strains is used. As a result, only three internal variables are needed to control the movement of the center of the switching surface in a kinematic hardening process. The model without that simplifying assumption is presented in Landis (2002). It is capable to simulate all hysteresis and butterfly loops including mechanical depolarization effects, which arise in ferroelectric ceramics.

Typical piezoelectric finite element models use displacements and the electric potential as nodal degrees of freedom, see Gaudenzi and Bathe (1995), Benjeddou (2000) and Klinkel and Wagner (2006) and the references therein. Accordingly the electric field and the strains are calculated from the gradients of the nodal degrees of freedom. With respect to the hysteresis effects the constitutive relations are highly nonlinear. Nonlinear problems are solved efficiently by applying the Newton–Raphson iteration scheme, which leads to a quadratic convergence. Therefore a consistent linearization of the weak form with respect to the unknown nodal degrees of freedom is necessary. This procedure is standard to solve problems with inelastic material behavior, see e.g. Simo and Hughes (1998). Due to the fact that the ferroelectric material models discussed above employ the irreversible polarization and the irreversible strain as internal variables a change of variables is necessary. Referring to Ghandi and Hagood (1997), it is very difficult to find a closed form for switching the variables, especially for non-linear material behavior including hysteretic response of the material. To circumvent a transformation of the variables Ghandi and Hagood (1997) suggested a hybrid finite element formulation, which incorporates electric displacement degrees of freedom as well as the conventional displacement and electric potential degrees of freedom. In Kamlah and Böhle (2001) the finite element analysis is carried out in a two-step scheme to avoid a switch of variables. In the first step a purely dielectric boundary problem is solved to obtain the electric potential. Secondly the electro-mechanical problem for the mechanical boundary conditions is analyzed with the prescribed electric potential. Zeng et al. (2003) use also a staggered scheme to solve the problem. For the finite element equations they employed Newton's method, for the analysis of the domain switching process an incremental approach is used. However, no convergence rates which could prove the quality of the proposed iteration scheme are shown in their paper.

In the present paper a thermodynamic consistent constitutive model which employs irreversible strains and irreversible electric field as internal variables is developed. The model fits perfectly in the finite element solution strategies for inelastic materials. A change of variables is not necessary. A consistent linearization is possible and the coupled electro mechanical boundary value problem is solved within one iterative solution procedure. The main features and the novel aspects of the present paper may be summarized as follows:

- A phenomenological macroscopic constitutive law based on a thermodynamically framework is derived. The formulation is based on the Helmholtz free energy and a scalar valued switching surface, which controls domain switching. In the framework of a kinematic hardening process the movement of the center of the switching surface is determined by internal variables.
- For the internal variables the irreversible strain is used and an irreversible electric field is introduced. This makes the formulation very useful for finite element implementation, where displacement and electric potential are the nodal degree of freedoms. From a computational view the formulation is very similar to plasticity theory, where the strains are additively split into a reversible and an irreversible part.
- No one-to-one relation between the irreversible strain and the polarization is employed. The domain switching process, which occurs due to an applied electric field, leads to an irreversible strain. The irreversible strains are additively split to accomplish "enough space" for the current level of polarization. It is distinguished between irreversible strains which occur due to stress application and irreversible strains which arise from a polarization process, see Kamlah and Tsakmakis (1999). For the latter one and for the irreversible electric field a special hardening function is introduced. The hardening function implies that

the irreversible strain is proportional to the deviatoric part of the dyadic product of the irreversible electric field.

- In the paper a consistent finite element implementation in a hexahedral eight-noded brick finite element is provided. Therefore the evolution equations for the internal variables are integrated by an implicit integration algorithm which leads to a local iteration. The iteration provides the stress and dielectric displacement for the residual vector. Furthermore an algorithmic consistent tangent modulus has to be considered to obtain quadratic convergence within the finite element calculation. In the present paper a numerical differentiation to evaluate the consistent tangent modulus is employed.
- The formulation accounts for the ferroelastic, the ferroelectric and the butterfly hysteresis as well as for mechanical depolarization effect.

The outline of the paper is as follows: In Section 2 the gradient fields are defined and the basic assumptions for the irreversible quantities are introduced. Section 3 represents the thermodynamical frame work and an implicit time integration algorithm of the evolution equations. In Section 4 the variational formulation and in Section 5 the finite element implementation are provided. The numerical examples in Section 6 show the capabilities and the main characteristics of the proposed model.

2. Gradient fields

In this section the electric field and the mechanical strains are defined. In the framework of a geometrically linear theory the strain tensor is given as

$$\boldsymbol{E} = \frac{1}{2}(\nabla \otimes \boldsymbol{u} + \boldsymbol{u} \otimes \nabla), \tag{1}$$

where $\boldsymbol{u}$ is the displacement vector and $\nabla = \partial/\partial \boldsymbol{X}$ is the Nabla-operator where $\boldsymbol{X} = [X_1, X_2, X_3]^{\mathrm{T}}$ is the position vector of the undeformed configuration. The total strain is additively decomposed as

$$\boldsymbol{E} = \boldsymbol{E}^{\mathrm{r}} + \boldsymbol{E}^{\mathrm{i}}. \tag{2}$$

Here $\boldsymbol{E}^{\mathrm{r}}$ represents the reversible part and $\boldsymbol{E}^{\mathrm{i}}$ is the irreversible strain, which occurs due to domain switching. The additive decomposition is exemplarily illustrated for the X_1-direction in Fig. 1. For $S_{11} = 0$ and $E_{11} = 0$ an unpolarized ceramic is assumed. At this state the material consists out of subregions of equal spontaneous polarization, the so called domains. Macroscopically an isotropic state with no resultant polarization and no piezoelectricity is observed. Increasing the stress up to the coercive stress S_c domain switching starts, see Fig. 1 point A. During the switching process the domains are aligned in tension direction, which results in an irreversible strain E^{i}_{11} The process stops when all domains are switched, in Fig. 1 point B is reached. At this point the total strain E_{11} consists of a reversible strain and of the maximum irreversible strain $E^{\mathrm{i}}_{11} = E^{\mathrm{i}}_{\mathrm{s}}$. The saturation strain $E^{\mathrm{i}}_{\mathrm{s}}$ for tension is twice as large as for compression, see e.g. Hwang and

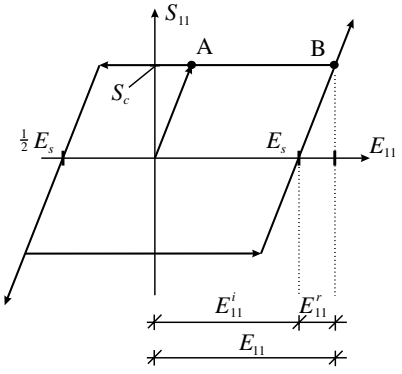

Fig. 1. Idealized ferroelastic hysteresis.

McMeeking (1999). It is noted that this state has no resultant polarization. In the absence of an electric field the stress tensor is obtained as

$$\boldsymbol{S} = \mathbb{C} : (\boldsymbol{E} - \boldsymbol{E}^{\mathrm{i}}), \tag{3}$$

where $\mathbb{C}$ denotes the elasticity tensor.

The Maxwell–Faraday theory of electrostatics postulates that the electric field $\vec{\boldsymbol{E}}$ is lamellar. In other words the postulate says that $\nabla \times \vec{\boldsymbol{E}} = 0$. This requirement is always fulfilled if the electric field is defined as

$$\vec{\boldsymbol{E}} = -\nabla\varphi, \tag{4}$$

where φ denotes the electric potential. An irreversible electric field is introduced with similar arguments as discussed for the ferroelastic hysteresis. In Fig. 2 an idealized dielectric hysteresis is shown, here the dielectric displacement in X_1-direction is denoted as $\vec{\boldsymbol{D}}_1$. At the point of origin an unpolarized ceramic is assumed where the domains are arbitrarily arranged. On a macroscopic level no resultant polarization appears. As long as the applied electric field is smaller than the coercive field $\vec{E}_{\mathrm{c}}$ the material behaves reversible and is characterized by the dielectric constant ϵ. Alternatively a coercive polarization $\vec{P}_{\mathrm{c}} = \epsilon\vec{E}_{\mathrm{c}}$ is introduced. The domain switching and therefore the polarization process starts at point A and ends at point B, see Fig. 2. The maximum irreversible polarization $\vec{P}_1$ is the saturation polarization $\vec{P}_{\mathrm{s}}$. Alternatively to $\vec{P}_{\mathrm{s}}$ an irreversible saturation field is defined as $\vec{E}^{\mathrm{i}}_{\mathrm{s}} := \vec{P}_{\mathrm{s}}/\epsilon$. This implies the idea of an irreversible electric field $\vec{E}^{\mathrm{i}}$.

In the absence of strain $\boldsymbol{E} = \boldsymbol{0}$ the difference of the applied electric field and the irreversible electric field multiplied with $\boldsymbol{\epsilon}$, a matrix containing dielectric constants, yields the dielectric displacement

$$\vec{\boldsymbol{D}} = \boldsymbol{\epsilon}(\vec{\boldsymbol{E}} - \vec{\boldsymbol{E}}^{\mathrm{i}}). \tag{5}$$

Accordingly the polarization vector is defined as

$$\vec{\boldsymbol{P}} = -\boldsymbol{\epsilon}\vec{\boldsymbol{E}}^{\mathrm{i}}. \tag{6}$$

This holds for an arbitrary point in the dielectric hysteresis. Within this formulation the irreversible electric field controls the polarization state. The evolution of the irreversible electric field is derived in Section 3 in a thermodynamically consistent framework. It is noted that $\vec{\boldsymbol{E}}^{\mathrm{i}}$ is introduced as a theoretically quantity without a physical meaning. Nevertheless we try to motivate this quantity form a physical point of view.

Therefore the polarization state of the ferroelectric ceramic at points A and B of Fig. 2 is analyzed in detail. Applying an increasing electric field $\vec{E}_1$ one obtains from the hysteresis loop that $\vec{E}^{\mathrm{i}}_1$ equals to zero at point A and increases up to $\vec{E}^{\mathrm{i}}_1 = -\vec{E}^{\mathrm{i}}_{\mathrm{s}}$ at point B. Which means that in general the direction of $\vec{\boldsymbol{E}}^{\mathrm{i}}$ is contrary to the electric field $\vec{\boldsymbol{E}}$. To motivate the irreversible electric field physically Fig. 3 shows the piezoelectric ceramic before the polarization and after polarization. The points A and B refer to the dielectric hysteresis in Fig. 2. Due to domain switching positive and negative charges are obtained beneath the surface of the ceramic. The material is now polarized and an internal electric field $\vec{E}^{\mathrm{i}}$ arises. In the literature the internal electric field $\vec{E}^{\mathrm{i}}_1 = -\vec{P}_1/\epsilon$ is also denoted as depolarizing field, see e.g. Ikeda (1990). It is obvious that it has a contrary direction to $\vec{E}$, $\vec{D}$ and $\vec{P}$.

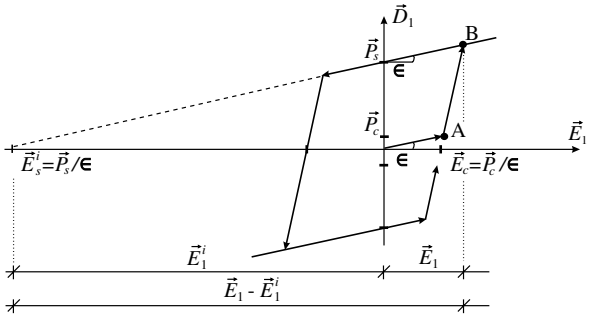

Fig. 2. Idealized dielectric hysteresis.

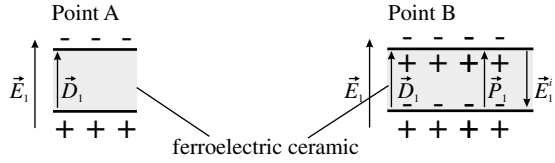

Fig. 3. Ferroelectric ceramic with positive and negative charges.

In the present contribution a uni-axial model embedded in a three-dimensional formulation is presented. It is assumed that polarization arise only along a given direction $\boldsymbol{e}_{\mathrm{p}}$, where the vector $\boldsymbol{e}_{\mathrm{p}}$, is normalized. The structural tensor

$$\boldsymbol{M} = \boldsymbol{e}_{\mathrm{p}} \otimes \boldsymbol{e}_{\mathrm{p}} \tag{7}$$

characterizes the polarization direction in the underlying constitutive equation.

3. Thermodynamic framework

In this section the constitutive law is developed for non magnetizable polycrystalline ferroelectric ceramics under isothermal conditions for rate independent deformation and polarization processes. Electric induced contributions to the balance of momentum and angular momentum are not considered in the present work, which means that ponderomotoric forces are neglected and the stress tensor is assumed to be symmetric; for detailed discussion see Maugin (1988) and Eringen and Maugin (1990). Similar to Bassiouny et al. (1988a) a thermodynamic potential which acts as an enthalpy function is defined as free energy per unit volume and is introduced as

$$\psi = \frac{1}{2}(\boldsymbol{E} - \boldsymbol{E}^{\mathrm{i}}) : \mathbb{C} : (\boldsymbol{E} - \boldsymbol{E}^{\mathrm{i}}) + \frac{\vec{\boldsymbol{E}}^{\mathrm{i}} \cdot \boldsymbol{e}_{\mathrm{p}}}{\vec{E}^{\mathrm{i}}_{\mathrm{s}}} \vec{\boldsymbol{E}} \cdot \mathbb{e} : (\boldsymbol{E} - \boldsymbol{E}^{\mathrm{i}}) - \frac{1}{2}(\vec{\boldsymbol{E}} - \vec{\boldsymbol{E}}^{\mathrm{i}}) \cdot \boldsymbol{\epsilon}(\vec{\boldsymbol{E}} - \vec{\boldsymbol{E}}^{\mathrm{i}}) + \bar{\psi}(\boldsymbol{E}^{\mathrm{i}}, \vec{\boldsymbol{E}}^{\mathrm{i}}). \tag{8}$$

Here, $\mathbb{C}$ is the elasticity tensor of rank four, $\mathbb{e}$ denotes the piezoelectric modulus of rank three and $\boldsymbol{\varepsilon}$ is the second order tensor of dielectric permittivity. The tensors are given within matrix representation in Appendix A. The free energy which is taken under consideration is restricted to be of second order, which means that it is quadratic in $\boldsymbol{E}$ and $\vec{\boldsymbol{E}}$. The initial reference configuration is assumed to be free of stress and dielectric displacement. The part $\bar{\psi}$ represents the free energy which is stored by the internal variables and may be interpreted as a hardening function. It depends only on the internal state variables of the material and is defined below. According to the second law of thermodynamics in the form of the Clausius–Duhem inequality neglecting thermal effects the dissipation inequality reads

$$\mathscr{D} = \boldsymbol{S} : \dot{\boldsymbol{E}} - \vec{\boldsymbol{D}} \cdot \dot{\vec{\boldsymbol{E}}} - \dot{\psi} \geqslant 0. \tag{9}$$

Here, $\boldsymbol{S}$ is the second order stress tensor and $\vec{\boldsymbol{D}}$ is the vector of dielectric displacements. The dot denotes the material time derivative. Applying standard arguments of rational continuum thermodynamics the following expressions for the stress and dielectric displacement are defined as

$$\begin{aligned} \boldsymbol{S} &:= \frac{\partial \psi}{\partial \boldsymbol{E}} = \mathbb{C} : (\boldsymbol{E} - \boldsymbol{E}^{\mathrm{i}}) + \frac{\vec{\boldsymbol{E}}^{\mathrm{i}} \cdot \boldsymbol{e}_{\mathrm{p}}}{\vec{E}^{\mathrm{i}}_{\mathrm{s}}} \mathbb{e}^{\mathrm{T}} \vec{\boldsymbol{E}}, \\ -\vec{\boldsymbol{D}} &:= \frac{\partial \psi}{\partial \vec{\boldsymbol{E}}} = \frac{\vec{\boldsymbol{E}}^{\mathrm{i}} \cdot \boldsymbol{e}_{\mathrm{p}}}{\vec{E}^{\mathrm{i}}_{\mathrm{s}}} \mathbb{e} : (\boldsymbol{E} - \boldsymbol{E}^{\mathrm{i}}) - \boldsymbol{\epsilon}(\vec{\boldsymbol{E}} - \vec{\boldsymbol{E}}^{\mathrm{i}}). \end{aligned} \tag{10}$$

With respect to this definitions the inequality (9) reduces to

$$\mathscr{D} = -\frac{\partial \psi}{\partial \boldsymbol{E}^{\mathrm{i}}} : \dot{\boldsymbol{E}}^{\mathrm{i}} - \frac{\partial \psi}{\partial \vec{\boldsymbol{E}}^{\mathrm{i}}} \cdot \dot{\vec{\boldsymbol{E}}}^{\mathrm{i}} \geqslant 0. \tag{11}$$

This inequality can be considered as a thermodynamical constraint imposed on the constitutive equations. Due to the fact that it depends not on the associated velocities $\dot{\boldsymbol{E}}$, $\dot{\vec{\boldsymbol{E}}}$ it represents instantaneous or rate independent dissipative processes. Eq. (11) motivates the definition of the work conjugate variables of the internal state variables as

$$\widehat{\boldsymbol{S}} := -\frac{\partial \psi}{\partial \boldsymbol{E}^{\mathrm{i}}} = \mathbb{C} : (\boldsymbol{E} - \boldsymbol{E}^{\mathrm{i}}) + \frac{\vec{\boldsymbol{E}}^{\mathrm{i}} \cdot \boldsymbol{e}_{\mathrm{p}}}{\vec{E}^{\mathrm{i}}_{\mathrm{s}}} \mathbb{e}^{\mathrm{T}} \vec{\boldsymbol{E}} - \frac{\partial \bar{\psi}}{\partial \boldsymbol{E}^{\mathrm{i}}} = \boldsymbol{S} - \frac{\partial \bar{\psi}}{\partial \boldsymbol{E}^{\mathrm{i}}}, \tag{12}$$

$$\widehat{\boldsymbol{D}} := -\frac{\partial \psi}{\partial \vec{\boldsymbol{E}}^{\mathrm{i}}} = -\frac{\vec{\boldsymbol{E}} \cdot \mathbb{e} : (\boldsymbol{E} - \boldsymbol{E}^{\mathrm{i}})}{E^{\mathrm{i}}_{\mathrm{s}}} \boldsymbol{e}_{\mathrm{p}} - \epsilon(\vec{\boldsymbol{E}} - \vec{\boldsymbol{E}}^{\mathrm{i}}) - \frac{\partial \bar{\psi}}{\partial \vec{\boldsymbol{E}}^{\mathrm{i}}} = -\frac{\vec{\boldsymbol{E}} \cdot \mathbb{e} : (\boldsymbol{E} - \boldsymbol{E}^{\mathrm{i}})}{\vec{E}^{\mathrm{i}}_{\mathrm{s}}} \boldsymbol{e}_{\mathrm{p}} - \epsilon \vec{\boldsymbol{E}} + \widehat{\boldsymbol{P}} - \frac{\partial \bar{\psi}}{\partial \vec{\boldsymbol{E}}^{\mathrm{i}}}. \tag{13}$$

The vector $\widehat{\boldsymbol{P}}$ is defined as $\widehat{\boldsymbol{P}} = \epsilon \vec{\boldsymbol{E}}^{\mathrm{i}}$ which is the negative polarization vector $\vec{\boldsymbol{P}}$. Rewriting the dissipation inequality (11) yields

$$\mathscr{D} = \widehat{\boldsymbol{S}} : \dot{\boldsymbol{E}}^{\mathrm{i}} + \widehat{\boldsymbol{D}} \cdot \dot{\vec{\boldsymbol{E}}}^{\mathrm{i}} \geqslant 0. \tag{14}$$

The postulate of the maximum dissipation with a switching surface as constraint is used to derive the evolution equations of the internal variables. The switching criterion ϕ controls domain switching and it holds $\phi < 0$ for reversible processes and $\phi = 0$ for irreversible processes. The switching criterion is defined as

$$\phi := \frac{3\widehat{\boldsymbol{S}} : \mathbb{P} : \widehat{\boldsymbol{S}}}{2S_{\mathrm{c}}^2} + \frac{(\widehat{\boldsymbol{D}} \cdot \boldsymbol{e}_{\mathrm{p}})^2}{\vec{P}_{\mathrm{c}}^2} + \xi \frac{f(\widehat{\boldsymbol{P}} \cdot \widehat{\boldsymbol{P}})}{S_{\mathrm{c}}^2 \vec{P}_{\mathrm{s}}^2} - 1 \leqslant 0 \tag{15}$$

with the fourth order deviatoric projection tensor $\mathbb{P} = \mathbb{I} - \frac{1}{3}\mathbf{1} \otimes \mathbf{1}$ and the fourth and second order identities $\mathbb{I}$, $\mathbf{1}$ respectively. The coercive values S_{c}, $\vec{P}_{\mathrm{c}}$ and the saturation polarization $\vec{P}_{\mathrm{s}}$ are material parameters, see also the discussion in Section 2. The first term in the switching criterion is formulated similarly to Landis (2002) and determines the ferroelastic hysteresis. Due to the fact that for ferroelectric ceramics the domain switching is volume preserving it is formulated in deviatoric quantities. The second term in Eq. (15) controls the ferroelectric and the butterfly hysteresis and the third term accounts for the mechanical depolarization effects. For the latter one the material parameter ξ is introduced to fit the mechanical depolarization behavior. With respect that mechanical depolarization occurs only in polarized ceramics which are subjected to a compression stress the function f is defined as

$$\begin{aligned} f &= \left(\tfrac{3}{2}\boldsymbol{S} : \mathbb{P} : \boldsymbol{M}\right)^2 \quad \text{if } \boldsymbol{S} : \mathbb{P} : \boldsymbol{M} < 0, \\ f &= 0 \qquad\qquad\qquad\quad \text{if } \boldsymbol{S} : \mathbb{P} : \boldsymbol{M} \geqslant 0. \end{aligned} \tag{16}$$

Eq. (16) states that the function f is greater than zero if there exists a compression stress, which is aligned to the polarization direction $\boldsymbol{e}_{\mathrm{p}}$. It is noted that the mechanical depolarization process is volume preserving, hence the deviatoric projection is employed for the function f. For the switching criterion the quantities $\widehat{\boldsymbol{S}} : \widehat{\vec{\boldsymbol{D}}}$, $\boldsymbol{S}$ and $\widehat{\boldsymbol{P}}$ are employed. Considering the relations (12) and (13) the stress $\boldsymbol{S}$ and the vector $\widehat{\boldsymbol{P}}$ may be seen as functions of the variables $\widehat{\boldsymbol{S}}$ and $\widehat{\boldsymbol{D}}$. A mathematical description of the optimization problem with constraint is given with the Lagrange function

$$\mathscr{L} = -\mathscr{D}(\widehat{\boldsymbol{S}}, \widehat{\boldsymbol{D}}) + \lambda \phi(\widehat{\boldsymbol{S}}, \widehat{\boldsymbol{D}}), \tag{17}$$

where λ is the Lagrange multiplier. For an optimization with an inequality as constraint the Kuhn–Tucker conditions require that

$$\frac{\partial \mathscr{L}}{\partial \widehat{\boldsymbol{S}}} = 0, \qquad \frac{\partial \mathscr{L}}{\partial \widehat{\boldsymbol{D}}} = 0, \qquad \frac{\partial \mathscr{L}}{\partial \lambda} = \phi = 0 \tag{18}$$

along with the loading conditions

$$\lambda \geqslant 0, \qquad \phi \leqslant 0, \qquad \lambda \phi = 0. \tag{19}$$

The clear meaning of the postulate of maximum dissipation is that for an irreversible state which is characterized by a given strain $\boldsymbol{E}$ and a given electric field $\vec{\boldsymbol{E}}$ that state of internal variables $\boldsymbol{E}^{\mathrm{i}}$, $\vec{\boldsymbol{E}}^{\mathrm{i}}$ has to be reached,

which maximizes the dissipation. From Eqs. (18), the evolution equations for the internal variables are derived as

$$\dot{\boldsymbol{E}}^{\mathrm{i}} = \lambda \frac{\partial \phi}{\partial \widehat{\boldsymbol{S}}} = \lambda \frac{3}{S_{\mathrm{c}}^2} \mathbb{P} : \widehat{\boldsymbol{S}} + \lambda \xi \frac{1}{S_{\mathrm{c}}^2 \vec{P}_{\mathrm{s}}^2} (\widehat{\boldsymbol{P}} \cdot \boldsymbol{e}_{\mathrm{p}})^2 \frac{\partial f}{\partial \widehat{\boldsymbol{S}}}, \tag{20}$$

$$\dot{\vec{\boldsymbol{E}}}^{\mathrm{i}} = \lambda \frac{\partial \phi}{\partial \widehat{\boldsymbol{D}}} = \lambda \frac{2}{\vec{P}_{\mathrm{c}}^2} (\widehat{\boldsymbol{D}} \cdot \boldsymbol{e}_{\mathrm{p}}) \boldsymbol{e}_{\mathrm{p}} + \lambda \xi \frac{2}{S_{\mathrm{c}}^2 \vec{P}_{\mathrm{s}}^2} f (\vec{\boldsymbol{P}} \cdot \boldsymbol{e}_{\mathrm{p}}) \boldsymbol{e}_{\mathrm{p}}. \tag{21}$$

For the derivative of f holds

$$\begin{aligned} \frac{\partial f}{\partial \widehat{\boldsymbol{S}}} &= 3 \left(\frac{3}{2} \boldsymbol{S} : \mathbb{P} : \boldsymbol{M} \right) \mathbb{P} : \boldsymbol{M} \quad \text{if } \boldsymbol{S} : \mathbb{P} : \boldsymbol{M} < 0, \\ \frac{\partial f}{\partial \widehat{\boldsymbol{S}}} &= 0 \qquad\qquad\qquad\qquad\quad \text{if } \boldsymbol{S} : \mathbb{P} : \boldsymbol{M} \geqslant 0. \end{aligned} \tag{22}$$

With respect to Eqs. (20) and (22) it is obvious that only deviatoric irreversible strain occur during domain switching. It is distinguished between the strain which arises due to mechanical depolarization $\dot{\boldsymbol{E}}^{\mathrm{Si}}$ and irreversible strains which occur because of dielectric or ferroelastic domain switching effects $\dot{\boldsymbol{E}}^{\mathrm{Pi}}$. This implies the additive decomposition

$$\dot{\boldsymbol{E}}^{\mathrm{i}} = \dot{\boldsymbol{E}}^{\mathrm{Pi}} + \dot{\boldsymbol{E}}^{\mathrm{Si}}, \tag{23}$$

with

$$\dot{\boldsymbol{E}}^{\mathrm{Pi}} = \lambda \frac{3}{S_{\mathrm{c}}^2} \mathbb{P} : \widehat{\boldsymbol{S}}, \tag{24}$$

$$\dot{\boldsymbol{E}}^{\mathrm{Si}} = \lambda \xi \frac{1}{S_{\mathrm{c}}^2 \vec{P}_{\mathrm{s}}^2} (\widehat{\boldsymbol{P}} \cdot \boldsymbol{e}_{\mathrm{p}})^2 \frac{\partial f}{\partial \widehat{\boldsymbol{S}}}. \tag{25}$$

An irreversible strain $\boldsymbol{E}^{\mathrm{Si}}$ occurs only if a compression stress is aligned to the polarization direction and thus $\partial f / \partial \widehat{\boldsymbol{S}} \neq \boldsymbol{0}$. It is remarked that $\boldsymbol{E}^{\mathrm{Si}}$ represents only the mechanical depolarization effect and has nothing to do with the ferroelastic hysteresis.

With respect to Eq. (21) one obtains that the irreversible electric field evolves in the direction of $\boldsymbol{e}_{\mathrm{p}}$. Considering $\beta := \vec{\boldsymbol{E}}^{\mathrm{i}} \cdot \boldsymbol{e}_{\mathrm{p}}$ results in a scalar valued function

$$\dot{\beta} = \lambda \frac{2}{\vec{P}_{\mathrm{c}}^2} (\widehat{\boldsymbol{D}} \cdot \boldsymbol{e}_{\mathrm{p}}) + \lambda \xi \frac{2}{S_{\mathrm{c}}^2 \vec{P}_{\mathrm{s}}^2} f (\widehat{\boldsymbol{P}} \cdot \boldsymbol{e}_{\mathrm{p}}). \tag{26}$$

3.1. Integration algorithm

The constitutive model is purely local and has to be integrated in time. Here, a time integration for the evolution equations is used which is in accordance with the a numerical solution of the irreversible boundary value problem by the finite element method employing displacements and electric potential as nodal degrees of freedom. The time integration schemes for rate independent plasticity in the context of finite element procedures are extensively discussed in the literature, see Simo and Hughes (1998) and Simo (1998) and the references therein. Here, it is assumed that the local state of the body at the time t_n is completely known. For a given displacement increment $\Delta \boldsymbol{u}$ and an increment of the electric potential $\Delta \varphi$ the state of the body at the time $t_{n+1} = t_n + \Delta t$ has to be determined. The basic problem is the update of the internal variables to time t_{n+1} for a prescribed total strain and total electric field. The problem is illustrated in Fig. 4.

The three evolution Eqs. (21), (24) and (25) are integrated by employing the backward Euler implicit integration scheme, which is unconditionally stable. For the integration we consider the time interval $[t_{n+1}, t_n]$; all quantities at the time t_n, t_{n+1} are denoted with the index n and $n+1$, respectively. The discrete forms of the evolution equations read

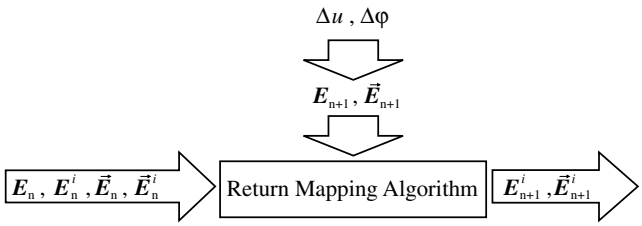

Fig. 4. Local return mapping algorithm, see also Simo and Hughes (1998).

$$
\begin{aligned}
\boldsymbol{E}_{n+1}^{\mathrm{Pi}} &= \boldsymbol{E}_n^{\mathrm{Pi}} + \gamma \frac{3}{S_{\mathrm{c}}^2} \mathbb{P} : \widehat{\boldsymbol{S}}_{n+1}, \\
\boldsymbol{E}_{n+1}^{\mathrm{Si}} &= \boldsymbol{E}_n^{\mathrm{Si}} + \gamma\xi \frac{1}{S_{\mathrm{c}}^2 \vec{P}_{\mathrm{s}}^2} (\widehat{\boldsymbol{P}}_{n+1} \cdot \boldsymbol{e}_{\mathrm{p}})^2 \frac{\partial f_{n+1}}{\partial \widehat{\boldsymbol{S}}_{n+1}}, \\
\beta_{n+1} &= \beta_n + \gamma \frac{2}{\vec{P}_{\mathrm{c}}^2} (\widehat{\boldsymbol{D}}_{n+1} \cdot \boldsymbol{e}_{\mathrm{p}}) + \gamma\xi \frac{2}{S_{\mathrm{c}}^2 \vec{P}_{\mathrm{s}}^2} f_{n+1} (\widehat{\boldsymbol{P}}_{n+1} \cdot \boldsymbol{e}_{\mathrm{p}}),
\end{aligned}
\tag{27}
$$

here γ is given by $\gamma = (t_{n+1} - t_n)\lambda$. For irreversible processes the switching surface has to fulfill $\phi_{n+1} = 0$. The switching surface and Eqs. (27) depend on $\widehat{\boldsymbol{S}}_{n+1}$, $\widehat{\vec{\boldsymbol{D}}}_{n+1}$, $\boldsymbol{S}_{n+1}$, $\widehat{\boldsymbol{P}}_{n+1}$ and therefore they are functions of the irreversible quantities $\boldsymbol{E}_{n+1}^{\mathrm{i}}$, $\vec{\boldsymbol{E}}_{n+1}^{\mathrm{i}}$, which are unknown at the step t_{n+1}. For the first predictor step trial values are assumed, see Fig. 5. If the switching criterion based on the trial state is satisfied, the actual irreversible variables are the trail values. If not, a corrector step has to be performed by the return mapping algorithm. In the framework of a general mapping algorithm the following four residua are defined as

$$
\begin{aligned}
\boldsymbol{R}_a &= \boldsymbol{E}_{n+1}^{\mathrm{Pi}} - \boldsymbol{E}_n^{\mathrm{Pi}} - \gamma \frac{3}{S_{\mathrm{c}}^2} \widehat{\boldsymbol{S}}_{n+1}^D = \boldsymbol{0}, \\
\boldsymbol{R}_b &= \boldsymbol{E}_{n+1}^{\mathrm{Si}} - \boldsymbol{E}_n^{\mathrm{Si}} - \gamma\xi \frac{1}{S_{\mathrm{c}}^2 \vec{P}_{\mathrm{s}}^2} (\widehat{\boldsymbol{P}}_{n+1} \cdot \boldsymbol{e}_{\mathrm{p}})^2 \frac{\partial f_{n+1}}{\partial \widehat{\boldsymbol{S}}_{n+1}} = \boldsymbol{0}, \\
R_{\mathrm{c}} &= \beta_{n+1} - \beta_n - \gamma \frac{2}{\vec{P}_{\mathrm{c}}^2} (\widehat{\boldsymbol{D}}_{n+1} \cdot \boldsymbol{e}_{\mathrm{p}}) - \gamma\xi \frac{2}{S_{\mathrm{c}}^2 \vec{P}_{\mathrm{s}}^2} f_{n+1} (\widehat{\boldsymbol{P}}_{n+1} \cdot \boldsymbol{e}_{\mathrm{p}}) = 0, \\
R_d &= \frac{3 \widehat{\boldsymbol{S}}_{n+1}^D : \widehat{\boldsymbol{S}}_{n+1}^D}{2 S_{\mathrm{c}}^2} + \frac{(\widehat{\boldsymbol{D}}_{n+1} \cdot \boldsymbol{e}_{\mathrm{p}})^2}{\vec{P}_{\mathrm{c}}^2} + \xi \frac{f_{n+1} (\widehat{\boldsymbol{P}}_{n+1} \cdot \widehat{\boldsymbol{P}}_{n+1})}{S_{\mathrm{c}}^2 \vec{P}_{\mathrm{s}}^2} - 1 = 0.
\end{aligned}
\tag{28}
$$

These equations are solved iteratively within a local Newton-iteration

$$
\begin{aligned}
\frac{\partial \boldsymbol{R}_a^{(k)}}{\partial \boldsymbol{E}_{n+1}^{\mathrm{Pi}}} : \Delta \boldsymbol{E}^{\mathrm{Pi}} + \frac{\partial \boldsymbol{R}_a^{(k)}}{\partial \boldsymbol{E}_{n+1}^{\mathrm{Si}}} : \Delta \boldsymbol{E}^{\mathrm{Si}} + \frac{\partial \boldsymbol{R}_a^{(k)}}{\partial \beta_{n+1}} \Delta\beta + \frac{\partial \boldsymbol{R}_a^{(k)}}{\partial \gamma} \Delta\gamma &= -\boldsymbol{R}_a^{(k)}, \\
\frac{\partial \boldsymbol{R}_b^{(k)}}{\partial \boldsymbol{E}_{n+1}^{\mathrm{Pi}}} : \Delta \boldsymbol{E}^{\mathrm{Pi}} + \frac{\partial \boldsymbol{R}_b^{(k)}}{\partial \boldsymbol{E}_{n+1}^{\mathrm{Si}}} : \Delta \boldsymbol{E}^{\mathrm{Si}} + \frac{\partial \boldsymbol{R}_b^{(k)}}{\partial \beta_{n+1}} \Delta\beta + \frac{\partial \boldsymbol{R}_b^{(k)}}{\partial \gamma} \Delta\gamma &= -\boldsymbol{R}_b^{(k)}, \\
\frac{\partial R_{\mathrm{c}}^{(k)}}{\partial \boldsymbol{E}_{n+1}^{\mathrm{Pi}}} : \Delta \boldsymbol{E}^{\mathrm{Pi}} + \frac{\partial R_{\mathrm{c}}^{(k)}}{\partial \boldsymbol{E}_{n+1}^{\mathrm{Si}}} : \Delta \boldsymbol{E}^{\mathrm{Si}} + \frac{\partial R_{\mathrm{c}}^{(k)}}{\partial \beta_{n+1}} \Delta\beta + \frac{\partial R_{\mathrm{c}}^{(k)}}{\partial \gamma} \Delta\gamma &= -R_{\mathrm{c}}^{(k)}, \\
\frac{\partial R_d^{(k)}}{\partial \boldsymbol{E}_{n+1}^{\mathrm{Pi}}} : \Delta \boldsymbol{E}^{\mathrm{Pi}} + \frac{\partial R_d^{(k)}}{\partial \boldsymbol{E}_{n+1}^{\mathrm{Si}}} : \Delta \boldsymbol{E}^{\mathrm{Si}} + \frac{\partial R_d^{(k)}}{\partial \beta_{n+1}} \Delta\beta + \frac{\partial R_d^{(k)}}{\partial \gamma} \Delta\gamma &= -R_d^{(k)},
\end{aligned}
\tag{29}
$$

with

$$
\begin{aligned}
\boldsymbol{E}_{n+1}^{\mathrm{Pi}(k+1)} &= \boldsymbol{E}_{n+1}^{\mathrm{Pi}(k)} + \Delta \boldsymbol{E}^{\mathrm{Pi}}, \quad \boldsymbol{E}_{n+1}^{\mathrm{Si}(k+1)} = \boldsymbol{E}_{n+1}^{\mathrm{Si}(k)} + \Delta \boldsymbol{E}^{\mathrm{Si}}, \\
\vec{\boldsymbol{E}}_{n+1}^{i(k+1)} &= \vec{\boldsymbol{E}}_{n+1}^{i(k)} + \Delta\beta \boldsymbol{e}_{\mathrm{p}}, \quad \gamma^{(k+1)} = \gamma^{(k)} + \Delta\gamma,
\end{aligned}
\tag{30}
$$

start values: $\boldsymbol{E}_{n+1},\ \vec{\boldsymbol{E}}_{n+1},\ \boldsymbol{E}_n^{Pi},\ \boldsymbol{E}_n^{Si},\ \vec{\boldsymbol{E}}_n^{i}$

predictor step

$$\boldsymbol{E}_{n+1}^{Pi} = \boldsymbol{E}_n^{Pi}, \quad \boldsymbol{E}_{n+1}^{Si} = \boldsymbol{E}_n^{Si}, \quad \vec{\boldsymbol{E}}_{n+1}^{i} = \vec{\boldsymbol{E}}_n^{i}$$

compute: $\boldsymbol{S}_{n+1},\ \vec{\boldsymbol{D}}_{n+1},\ \hat{\boldsymbol{S}}_{n+1},\ \hat{\boldsymbol{D}}_{n+1},\ \hat{\boldsymbol{P}}_{n+1}$

if $\phi_{n+1} \leq \text{tol}$ then stop

corrector step

$$\gamma = 0,\ k = 0,\ \boldsymbol{R}_a^{(k)} = \boldsymbol{0},\ \boldsymbol{R}_b^{(k)} = \boldsymbol{0},\ R_c^{(k)} = 0,\ R_d^{(k)} = \phi_{n+1}$$

1.) solve Equation (29) for

$$\Delta\boldsymbol{E}^{Pi},\ \Delta\boldsymbol{E}^{Si},\ \Delta\beta,\ \Delta\gamma$$

2.) updating via Equations (30)

$$\boldsymbol{E}_{n+1}^{Pi\ (k+1)},\ \boldsymbol{E}_{n+1}^{Si\ (k+1)},\ \vec{\boldsymbol{E}}_{n+1}^{(k+1)},\ \gamma^{(k+1)}$$

3.) compute: $\boldsymbol{S}_{n+1}^{(k+1)},\ \vec{\boldsymbol{D}}_{n+1}^{(k+1)},\ \hat{\boldsymbol{S}}_{n+1}^{(k+1)},\ \hat{\boldsymbol{D}}_{n+1}^{(k+1)},\ \hat{\boldsymbol{P}}_{n+1}^{(k+1)}$

4.) compute: $\boldsymbol{R}_a^{(k+1)},\ \boldsymbol{R}_b^{(k+1)},\ R_c^{(k+1)},\ R_d^{(k+1)}$

5.) if $\|\boldsymbol{R}_a^{(k+1)}\|$ and $\|\boldsymbol{R}_b^{(k+1)}\|$ and $\|R_c^{(k+1)}\|$ and $\|R_d^{(k+1)}\| \leq \text{tol}$

then $\boldsymbol{E}_{n+1}^{Pi} = \boldsymbol{E}_{n+1}^{Pi\ (k+1)},\ \boldsymbol{E}_{n+1}^{Si} = \boldsymbol{E}_{n+1}^{Si\ (k+1)},$

$\vec{\boldsymbol{E}}_{n+1}^{i} = \vec{\boldsymbol{E}}_{n+1}^{i\ (k+1)},\ \gamma = \gamma^{(k+1)}$

stop

6.) $k = k + 1$ goto 1.

Fig. 5. Return mapping algorithm for rate independent domain switching in ferroelectric ceramics.

where the superscript (k) denotes the iteration step. The derivatives in Eqs. (29) are given in Appendix B. The irreversible electric field at the time step t_{n+1} is obtained by $\vec{\boldsymbol{E}}_{n+1}^{\mathrm{i}} = \beta_{n+1}\boldsymbol{e}_{\mathrm{p}}$. A summary of the return mapping algorithm is presented in Fig. 5.

3.2. Hardening functions

The last part of the free energy $\bar{\psi}$ acts as hardening function. With respect to the different hysteresis types it is split in three parts

$$\bar{\psi} = \overset{1}{\psi}(\boldsymbol{E}^{\mathrm{i}}) + \overset{2}{\psi}(\vec{\boldsymbol{E}}^{\mathrm{i}}) + \overset{3}{\psi}(\boldsymbol{E}^{\mathrm{Pi}}, \vec{\boldsymbol{E}}^{\mathrm{i}}). \tag{31}$$

The first part is a function of the total irreversible strain $\boldsymbol{E}^{\mathrm{i}} = \boldsymbol{E}^{\mathrm{Pi}} + \boldsymbol{E}^{\mathrm{Si}}$ and describes the ferroelastic hysteresis loop. The second part characterizes the dielectric hysteresis and is a function of the irreversible electric field. The third part considers coupling of irreversible electric field and strains and is responsible for the butterfly loop.

3.2.1. Ferroelastic hardening

The hardening function is formulated in principal strains, which is necessary to account for different irreversible deformation states. The following eigenvalue problem:

$$(\boldsymbol{E}^{\mathrm{i}} - E^{\mathrm{i}}_A \mathbf{1})\boldsymbol{N}_A = \mathbf{0} \tag{32}$$

provides the principal irreversible strains E^{i}_A along with the principal directions $\boldsymbol{N}_A$, where A runs from 1 to 3. For the eigenvectors hold $\boldsymbol{N}_A \cdot \boldsymbol{N}_B = \delta_{AB}$ with $A, B = 1, 2, 3$ and where δ_{AB} represents the Kronecker delta. With respect to Eqs. (12) and (24) the derivative of the hardening function is needed for the evolution equation. With the abbreviation $\alpha_A = E^{\mathrm{i}}_A / E^{\mathrm{i}}_{\mathrm{s}}$ and $E^{\mathrm{i}}_{\mathrm{s}}$ is the irreversible saturation strain along with the material parameters h, mc, mt the following function is defined as

$$\frac{\partial \overset{1}{\psi}}{\partial \boldsymbol{E}^{\mathrm{i}}} = \sum_{A=1}^{3} \underbrace{\frac{h E^{\mathrm{i}}_{\mathrm{s}} \alpha_A}{(1+2\alpha_A)^{mc}(1-\alpha_A)^{mt}}}_{\eta_A} \boldsymbol{N}_A \otimes \boldsymbol{N}_A \tag{33}$$

and was proposed in Landis (2002). The function restricts the value for α_A between $-0.5 < \alpha_A < 1.0$. This leads to a maximum irreversible compression strain $E^{\mathrm{i}}_A = -E^{\mathrm{i}}_{\mathrm{s}}/2$ and a maximal irreversible tension strain $E^{\mathrm{i}}_A = E^{\mathrm{i}}_{\mathrm{s}}$, which coincides with experimental data, see Fett et al. (1998). For the local iteration Eq. (29) the second derivative of the hardening function, see Appendix B, is necessary. Following Chadwick and Ogden (1971) it is provided as

$$\begin{aligned} \frac{\partial\partial \overset{1}{\psi}}{\partial \boldsymbol{E}^{\mathrm{i}} \partial \boldsymbol{E}^{\mathrm{i}}} &= \sum_{A=1}^{3} \frac{\partial \eta_A}{\partial \alpha_A} \boldsymbol{N}_A \otimes \boldsymbol{N}_A \otimes \boldsymbol{N}_A \otimes \boldsymbol{N}_A \\ &\quad + \sum_{A \neq B = 1}^{3} \frac{1}{2} \frac{\eta_A - \eta_B}{\alpha_A - \alpha_B} (\boldsymbol{N}_A \otimes \boldsymbol{N}_B \otimes \boldsymbol{N}_A \otimes \boldsymbol{N}_B + \boldsymbol{N}_A \otimes \boldsymbol{N}_B \otimes \boldsymbol{N}_B \otimes \boldsymbol{N}_A), \end{aligned} \tag{34}$$

with

$$\frac{\partial \eta_A}{\partial \alpha_A} = h \frac{(1+2\alpha_A)(1-\alpha_A) - 2\alpha_A(1-\alpha_A)mc + \alpha_A(1+2\alpha_A)mt}{(1+2\alpha_A)^{mc+1}(1-\alpha_A)^{mt+1}}. \tag{35}$$

3.2.2. Ferroelectric hardening

The second function in Eq. (31) determines only the dielectric hysteresis loop and not the butterfly loop. With the saturation electric field $\vec{E}^{\mathrm{i}}_{\mathrm{s}}$ and the material parameters k, a and b it is introduced as follows:

$$\overset{2}{\psi} = \frac{1}{2} k \beta^2 - a\beta \operatorname{arctanh}\left(\frac{\beta}{b\vec{E}^{\mathrm{i}}_{\mathrm{s}}}\right) + \frac{1}{2} ab\vec{E}^{\mathrm{i}}_{\mathrm{s}} \ln\left(1 - \frac{\beta^2}{b^2 \vec{E}^{\mathrm{i}}_{\mathrm{s}} 2}\right). \tag{36}$$

The first and the second derivative of Eq. (36) read

$$\begin{aligned} \frac{\partial \overset{2}{\psi}}{\partial \vec{\boldsymbol{E}}^{\mathrm{i}}} &= \left(k\beta + a \operatorname{arctanh}\left(\frac{\beta}{b\vec{E}^{\mathrm{i}}_{\mathrm{s}}}\right)\right) \boldsymbol{e}_{\mathrm{p}}, \\ \frac{\partial\partial \overset{2}{\psi}}{\partial \vec{\boldsymbol{E}}^{\mathrm{i}} \partial \vec{\boldsymbol{E}}^{\mathrm{i}}} &= \left(k + \frac{a}{1 - \left(\frac{\beta}{b\vec{E}^{\mathrm{i}}_{\mathrm{s}}}\right)^2} \frac{1}{b\vec{E}^{\mathrm{i}}_{\mathrm{s}}}\right) \boldsymbol{M}. \end{aligned} \tag{37}$$

3.2.3. Coupled ferroelectric hardening

To capture remanent straining effects and the mechanical depolarization the third hardening function is introduced. The task is to accomplish enough space in terms of irreversible strains during domain switching.

Ceramics like PZT undergo an increase in irreversible strain during the polarization by an applied electric field. A common assumption is the one-to-one relation between the polarization and the irreversible strains, see e.g. Kamlah (2001). In terms of the irreversible electric field this relation reads

$$\frac{3}{2}\frac{1}{\vec{E}_{\mathrm{s}}^{\mathrm{i}\,2}}(\vec{\boldsymbol{E}}^{\mathrm{i}}\otimes\vec{\boldsymbol{E}}^{\mathrm{i}}):\mathbb{P}-\frac{1}{E_{\mathrm{s}}^{\mathrm{i}}}\boldsymbol{E}^{\mathrm{i}}=0. \tag{38}$$

Applying this relation only to the irreversible electric field $\boldsymbol{E}^{\mathrm{pi}}$ which arise due to polarization and considering a projection on the polarization direction $\vec{\boldsymbol{E}}^{\mathrm{i}}=\beta\boldsymbol{e}_{\mathrm{p}}$ leads to

$$\left(\frac{\beta}{\vec{E}_{\mathrm{s}}^{\mathrm{i}}}\right)^{2}-\frac{1}{E_{\mathrm{s}}^{\mathrm{i}}}\boldsymbol{E}^{\mathrm{pi}}:\boldsymbol{M}=0. \tag{39}$$

This scalar valued relation is used as an argument for the following coupled hardening function:

$$\overset{3}{\psi}=\zeta\left(\frac{\beta}{\vec{E}_{\mathrm{s}}^{\mathrm{i}}}\right)^{2}\left(\cosh\left(\left(\frac{\beta}{\vec{E}_{\mathrm{s}}^{\mathrm{i}}}\right)^{2}-\frac{1}{E_{\mathrm{s}}^{\mathrm{i}}}\boldsymbol{E}^{\mathrm{pi}}:\boldsymbol{M}\right)-1\right), \tag{40}$$

here, ζ represents another material parameter. The derivatives of the hardening function are given as

$$\begin{aligned}\frac{\partial\overset{3}{\psi}}{\partial\vec{\boldsymbol{E}}^{\mathrm{i}}}&=\zeta\left(2\frac{\beta}{\vec{E}_{\mathrm{s}}^{i2}}(\cosh(q)-1)+2\frac{\beta^{3}}{\vec{E}_{\mathrm{s}}^{i4}}\sinh(q)\right)\boldsymbol{e}_{\mathrm{p}},\\ \frac{\partial\overset{2}{\psi}}{\partial\boldsymbol{E}^{\mathrm{i}}}&=-\zeta\frac{\beta^{2}}{E_{\mathrm{s}}^{\mathrm{i}}\vec{E}_{\mathrm{s}}^{i2}}\sinh(q)\boldsymbol{M},\end{aligned} \tag{41}$$

with $q=\left(\frac{\beta}{\vec{E}_{\mathrm{s}}^{\mathrm{i}}}\right)^{2}-\frac{1}{E_{\mathrm{s}}^{\mathrm{i}}}\boldsymbol{E}^{\mathrm{pi}}:\boldsymbol{M}$.

For the local iteration the second derivatives are provided as

$$\begin{aligned}\frac{\partial\partial\overset{3}{\psi}}{\partial\vec{\boldsymbol{E}}^{\mathrm{i}}\,\partial\vec{\boldsymbol{E}}^{\mathrm{i}}}&=\zeta\left(2\frac{1}{\vec{E}_{\mathrm{s}}^{i2}}(\cosh(q)-1)+10\frac{\beta^{2}}{\vec{E}_{\mathrm{s}}^{i4}}\sinh(q)+4\frac{\beta^{4}}{\vec{E}_{\mathrm{s}}^{i6}}\cosh(q)\right)\boldsymbol{M},\\ \frac{\partial\partial\overset{3}{\psi}}{\partial\vec{\boldsymbol{E}}^{\mathrm{i}}\,\partial\boldsymbol{E}^{\mathrm{pi}}}&=-\zeta\left(2\frac{\beta}{E_{\mathrm{s}}^{\mathrm{i}}\vec{E}_{\mathrm{s}}^{i2}}\sinh(q)+2\frac{\beta^{3}}{E_{\mathrm{s}}^{\mathrm{i}}\vec{E}_{\mathrm{s}}^{i4}}\cosh(q)\right)\boldsymbol{e}_{\mathrm{p}}\otimes\boldsymbol{M},\\ \frac{\partial\partial\overset{3}{\psi}}{\partial\boldsymbol{E}^{\mathrm{pi}}\,\partial\boldsymbol{E}^{\mathrm{pi}}}&=\zeta\left(\frac{\beta^{2}}{E_{\mathrm{s}}^{i2}\vec{E}_{\mathrm{s}}^{i2}}\cosh(q)\right)\boldsymbol{M}\otimes\boldsymbol{M}.\end{aligned} \tag{42}$$

4. Variational formulation

In this section the weak form of the governing equations for the coupled mixed field problem is provided. A mechanical force $\boldsymbol{t}$ or a displacement $\boldsymbol{u}$ may be applied to the boundary of a body $\mathscr{B}_0$, which is denoted with $\partial\mathscr{B}_{0u}$ and $\partial\mathscr{B}_{0t}$, respectively. It holds $\partial\mathscr{B}_0=\partial\mathscr{B}_{0u}\bigcup\partial\mathscr{B}_{0t}$ and $\emptyset=\partial\mathscr{B}_{0u}\bigcap\partial\mathscr{B}_{0t}$. With σ is the free electric surface charge one may distinguish between the boundary with given σ and with a given φ. Accordingly it holds $\partial\mathscr{B}_0=\partial\mathscr{B}_{0\varphi}\bigcup\partial\mathscr{B}_{0\sigma}$ and $\emptyset=\partial\mathscr{B}_{0\varphi}\bigcap\partial\mathscr{B}_{0\sigma}$. Furthermore it is assumed that the free charge density is given with κ; the body force is defined with $\boldsymbol{b}\rho_0$, where ρ_0 denotes the mass density. The governing field equations read

$$\boldsymbol{S}\nabla+\rho_0\boldsymbol{b}=0\quad\text{in }\mathscr{B}_0, \tag{43}$$

$$\vec{\boldsymbol{D}}\cdot\nabla-\kappa=0\quad\text{in }\mathscr{B}_0 \tag{44}$$

and the corresponding boundary conditions are given as

$$\boldsymbol{S}\boldsymbol{n} - \boldsymbol{t} = \boldsymbol{0} \quad \text{on } \partial\mathscr{B}_{0t}, \tag{45}$$

$$\vec{\boldsymbol{D}} \cdot \boldsymbol{n} - \sigma = 0 \quad \text{on } \partial\mathscr{B}_{0\sigma}, \tag{46}$$

where $\boldsymbol{n}$ denotes the normal outward vector on $\partial\mathscr{B}_0$. In particular Eq. (43) represents the local form of the balance of momentum and Eq. (44) is known as the local form of the Gauss' law. The stress tensor is in general not symmetric for non-linear materials. With respect to Voigt's piezoelectricity theory (Voigt, 1928) no ponderomotive forces are considered; therefore the stress tensor is symmetric by default and the balance law of moment of momentum is fulfilled. The boundary condition (45) defines the mechanical surface traction and Eq. (46) is a jump condition, where σ describes the external applied electric surface charge.

Let $\mathscr{U} := \{\delta\boldsymbol{u} \in [H^1(\mathscr{B}_0)]\delta\boldsymbol{u}|_{\partial\mathscr{B}_{0u}} = 0\}$ be the space of admissible virtual displacements and $\mathscr{V} := \{\delta\varphi \in [H^1(\mathscr{B}_0)]\delta\varphi|_{\partial\mathscr{B}_{0\varphi}} = 0\}$ be the space of the admissible virtual electric potential. The weak form is obtained, by multiplying Eqs. (43) and (44) with the test functions $\delta\boldsymbol{u}$ and $\delta\varphi$, respectively. Integration by parts and the use of the divergence theorem leads to

$$\delta\pi = \int_{\mathscr{B}_0} \left(\frac{\partial\psi}{\partial\boldsymbol{E}} : \delta\boldsymbol{E} + \frac{\partial\psi}{\partial\vec{\boldsymbol{E}}} \cdot \delta\vec{\boldsymbol{E}} \right) \mathrm{d}V - \int_{\mathscr{B}_0} \rho_0 \boldsymbol{b} \cdot \delta\boldsymbol{u}\, \mathrm{d}V - \int_{\partial\mathscr{B}_0} \boldsymbol{t} \cdot \delta\boldsymbol{u}\, \mathrm{d}A + \int_{\mathscr{B}_0} \kappa\delta\varphi\, \mathrm{d}V - \int_{\partial\mathscr{B}_0} \sigma\delta\varphi\, \mathrm{d}A = 0. \tag{47}$$

The virtual gradient fields are given with $\delta\boldsymbol{E} = \frac{1}{2}(\nabla \otimes \delta\boldsymbol{u} + \delta\boldsymbol{u} \otimes \nabla)$ and $\delta\vec{\boldsymbol{E}} = -\nabla\delta\varphi$.

It is remarked that within the weak form (47) the boundary conditions (45) and (46) are fulfilled. The remaining boundary condition for a prescribed displacement $\boldsymbol{u}_0$ and a prescribed electric potential φ_0

$$\boldsymbol{u} - \boldsymbol{u}_0 = \boldsymbol{0} \quad \text{on } \partial\mathscr{B}_{0u} \tag{48}$$

$$\varphi - \varphi_0 = 0 \quad \text{on } \partial\mathscr{B}_{0\varphi}, \tag{49}$$

have to be satisfied explicitly. Furthermore it is noted that the Clausius–Duhem inequality is enforced locally at each material point, see Section 3.

5. Finite element approximation

The finite element approximation is constructed by dividing the whole domain in element domains with $\mathscr{B}_0 = \bigcup_{e=1}^{\mathrm{nelm}} \mathscr{B}_e$ where nelm is the total number of elements. For a hexahedral element with eight nodes the trilinear shape function at the node I is given as

$$N_I = \frac{1}{8}(1 + \xi_I^1\xi^1)(1 + \xi_I^2\xi^2)(1 + \xi_I^3\xi^3) \quad \text{with } -1 \leqslant \xi^{\mathrm{i}} \leqslant +1 \tag{50}$$

and

$$\begin{aligned} \xi_I^1 &\in \{-1, \quad 1, \quad 1, \quad -1, \quad -1, \quad 1, \quad 1, \quad -1\}, \\ \xi_I^2 &\in \{-1, \quad -1, \quad 1, \quad 1, \quad -1, \quad -1, \quad 1, \quad 1\}, \\ \xi_I^3 &\in \{-1, \quad -1, \quad -1, \quad -1, \quad 1, \quad 1, \quad 1, \quad 1\}. \end{aligned} \tag{51}$$

The approximation of the geometry on element level (index e) reads

$$\boldsymbol{X}_e^h = \sum_{I=1}^{8} N_I \boldsymbol{X}_I. \tag{52}$$

The superscript h is the characteristic size of the finite element discretization and indicates the finite element approximation. The vector $\boldsymbol{X}_I$ contains the nodal co-ordinates. The interpolation functions N_I are arranged in the matrix $\boldsymbol{N} = [\boldsymbol{N}_1, \boldsymbol{N}_2, \boldsymbol{N}_3, \boldsymbol{N}_4, \boldsymbol{N}_5, \boldsymbol{N}_6, \boldsymbol{N}_7, \boldsymbol{N}_8]$ with $\boldsymbol{N}_I = \mathrm{diag}[N_I, N_I, N_I, N_I]$. By means of the isoparametric

concept the geometry, the displacements and the electric potential are approximated with the same interpolation functions as

$$\boldsymbol{d}_e^h = \begin{bmatrix} u_e^h \\ \varphi_e^h \end{bmatrix} = \boldsymbol{N}\boldsymbol{v}_e. \tag{53}$$

The vector $\boldsymbol{v}_e$ is defined as $\boldsymbol{v}_e = [\boldsymbol{u}_1^{\mathrm{T}}, \varphi_1, \boldsymbol{u}_2^{\mathrm{T}}, \varphi_2, \boldsymbol{u}_3^{\mathrm{T}}, \varphi_3, \boldsymbol{u}_4^{\mathrm{T}}, \varphi_4, \boldsymbol{u}_5^{\mathrm{T}}, \varphi_5, \boldsymbol{u}_6^{\mathrm{T}}, \varphi_6, \boldsymbol{u}_7^{\mathrm{T}}, \varphi_7, \boldsymbol{u}_8^{\mathrm{T}}, \varphi_8]^{\mathrm{T}}$. Considering the vector notation given in the appendix equation (A.1) the approximations of the gradient fields read

$$\begin{pmatrix} \boldsymbol{E}_e^h \\ \vec{\boldsymbol{E}}_e^h \end{pmatrix} = \boldsymbol{B}\boldsymbol{v}_e \quad \text{with } \boldsymbol{B} = [\boldsymbol{B}_1, \boldsymbol{B}_2, \boldsymbol{B}_3, \boldsymbol{B}_4, \boldsymbol{B}_5, \boldsymbol{B}_6, \boldsymbol{B}_7, \boldsymbol{B}_8]. \tag{54}$$

The B-matrix at the node I is given as

$$\boldsymbol{B}_I = \begin{bmatrix} \boldsymbol{B}_I^u & \boldsymbol{0} \\ 0 & \boldsymbol{B}_I^\varphi \end{bmatrix} \tag{55}$$

and

$$\boldsymbol{B}_I^u = \begin{bmatrix} N_{I,X_1} & 0 & 0 \\ 0 & N_{I,X_2} & 0 \\ 0 & 0 & N_{I,X_3} \\ N_{I,X_2} & N_{I,X_1} & 0 \\ N_{I,X_3} & 0 & N_{I,X_1} \\ 0 & N_{I,X_3} & N_{I,X_2} \end{bmatrix}, \qquad \boldsymbol{B}_I^\varphi = \begin{bmatrix} N_{I,X_1} \\ N_{I,X_2} \\ N_{I,X_3} \end{bmatrix}. \tag{56}$$

The derivative of the shape functions with respect to $\boldsymbol{X}$ is obtained with the Jacobian

$$\boldsymbol{J} = \nabla_\xi \otimes \boldsymbol{X}_e^h \quad \text{with } \nabla_\xi = \left[\frac{\partial}{\partial \xi^1} \frac{\partial}{\partial \xi^2} \frac{\partial}{\partial \xi^3}\right]^{\mathrm{T}} \tag{57}$$

as

$$\nabla N_I = \boldsymbol{J}^{-1} \nabla_\xi N_I. \tag{58}$$

The interpolations (53) and (54) hold also for the variations. Taken into account the vector and matrix notation in Appendix A the approximation of the weak form equation (47) is observed on element level as

$$\delta\pi_e^h = \delta\boldsymbol{v}_e^{\mathrm{T}} \underbrace{\left[\int_{\mathscr{B}_e} \left(\boldsymbol{B}^{\mathrm{T}} \begin{pmatrix} \frac{\partial \psi}{\partial \boldsymbol{E}} \\ \frac{\partial \psi}{\partial \vec{\boldsymbol{E}}} \end{pmatrix} - \boldsymbol{N}^{\mathrm{T}} \begin{pmatrix} \rho_0 \boldsymbol{b} \\ \kappa \end{pmatrix} \right) \mathrm{d}V - \int_{\partial\mathscr{B}_e} \boldsymbol{N}^{\mathrm{T}} \begin{pmatrix} \boldsymbol{t} \\ \sigma \end{pmatrix} \mathrm{d}A \right]}_{\boldsymbol{R}_e^h}. \tag{59}$$

After assembly over all elements one obtains $\delta\pi^h = \mathsf{A}_{e=1}^{\mathrm{nelm}} \delta\pi_e^h$, the residual vector $\boldsymbol{R}^h = \mathsf{A}_{e=1}^{\mathrm{nelm}} \boldsymbol{R}_e^h$ and $\boldsymbol{v}^h = \mathsf{A}_{e=1}^{\mathrm{nelm}} \boldsymbol{v}_e^h$. Due to the fact that ψ is a nonlinear function of φ and $\boldsymbol{u}$ the equation $\delta\pi^h = 0$ is solved iteratively.

5.1. Algorithmic consistent tangent modulus

Quadratic convergence is obtained by employing the Newton–Raphson scheme to solve the problem iteratively within the finite element method. During the load step $[t_{n+1}, t_n]$ the residual vector (59) at t_{n+1} is expanded in a Taylor series, which is truncated after the linear element

$$\boldsymbol{R}_{n+1}^{h(k)} + \frac{\partial \boldsymbol{R}_{n+1}^{h(k)}}{\partial \boldsymbol{d}_{n+1}} \Delta \boldsymbol{d}_{n+1}^{(k)} = 0. \tag{60}$$

The nodal degrees of freedom are determined by $\boldsymbol{d}_{n+1}^{(k+1)} = \boldsymbol{d}_{n+1}^{(k)} + \Delta\boldsymbol{d}_{n+1}^{(k+1)}$, where the superscript (k) denotes the iteration step. The last equilibrium state is considered as start value for the first iteration and reads $\boldsymbol{d}_{n+1}^{(1)} = \boldsymbol{d}_n$. Applying the chain rule Eq. (60) yields the tangent stiff matrix

$$\boldsymbol{K}_{e\mathrm{T}} := \frac{\partial \boldsymbol{R}_{en+1}^{h(k)}}{\partial \boldsymbol{d}_{n+1}} = \int_{\mathscr{L}_e} \boldsymbol{B}^{\mathrm{T}} \mathbb{D}_{\mathrm{T}} \boldsymbol{B} \mathrm{d}X, \quad \mathbb{D}_{\mathrm{T}} = \begin{bmatrix} \dfrac{\partial\partial\psi}{\partial\boldsymbol{E}\partial\boldsymbol{E}} & \dfrac{\partial\partial\psi}{\partial\boldsymbol{E}\partial\vec{\boldsymbol{E}}} \\ \dfrac{\partial\partial\psi}{\partial\vec{\boldsymbol{E}}\partial\boldsymbol{E}} & \dfrac{\partial\partial\psi}{\partial\vec{\boldsymbol{E}}\partial\vec{\boldsymbol{E}}} \end{bmatrix}_{n+1}^{(k)}, \tag{61}$$

where $\mathbb{D}_{\mathrm{T}}$ is the algorithmic consistent tangent modulus. Here a numerical differentiation for the evaluation of the tangent modulus is employed, see e.g. Wriggers (2001).

6. Numerical examples

The finite element formulation is implemented in a modified version of the finite element analysis program FEAP developed by Taylor.[1] One aspect which is discussed within the numerical examples is the numerical behavior of the proposed formulation. Regarding to the local and global Newton iteration schemes a quadratic convergence is expected. Another focus is the numerical simulation of experimental data, which confirms the capability of the present model.

In the first example the overall behavior of ferroelectric ceramics is analyzed. This includes the prediction of the ferroelastic hysteresis as well as the dielectric hysteresis along with the butterfly loop. Furthermore it is shown that the model accounts also for mechanical depolarization of an initially polarized piezoelectric sample. The numerical behavior of a representative load step is investigated with respect to the convergence rate of the different residua.

In the second example experimental data of lead lanthanum zirconate titanate is simulated with the proposed model. A proper choice of the different material parameters, which are included in the hardening functions and the switching criteria, is provided. The example shows that an appropriate choice of the material parameters is possible.

The third examples is concerned with non-remanent straining ferroelectric ceramics. For this materials no remanent strain is obtained for a polarized ceramic when the electric field is removed. Consequently the polarization is not coupled with the irreversible strain. In the present constitutive formulation the coupling between the irreversible electric field and the irreversible strains can be weakened by deactivating the third hardening function (40). A simulation of the corresponding dielectric hysteresis and butterfly loop is presented.

In the last example a cantilever beam is polarized in the direction of the beam axis afterwards it is subjected to a transverse tip force. The force leads to a mechanical depolarization of particular regions in the cantilever. Within the example the location in the beam and the intensity of the arising mechanical depolarization are discussed. The non-linear impact on the deflection of the beam is illustrated.

6.1. Hysteresis loops in ferroelectric ceramics

In the first example the approximations of the different hysteresis loops by the proposed model are discussed. The convergence behavior of the global and local iterations are presented.

A cube with an edge length of $L = 10$ mm is subjected to either an mechanical force F or an electric potential φ. The boundary conditions are shown in Fig. 6. The material parameters are chosen as a rough approximation of soft PZT and are summarized in Table 1.

In the first load case a force F is applied to the free end of the rod. The force is increased up to $F = 2.5$ kN; afterwards decreased to the minimum of $F = -2.5$ kN and then again increased to the value $F = 1.25$ kN. The result is a ferroelastic hysteresis curve, which is depicted in Fig. 7. The strain at the x-axis is normalized by the irreversible saturation strain. It is observed that the irreversible strain E_{33}, which results from tension, is equal to the saturation strain, whereas a compression stress leads to a maximum irreversible strain which is half as

[1] Taylor, R.L., Feap-manual. http://www.ce.berkeley/~rlt/feap/manual.pdf.

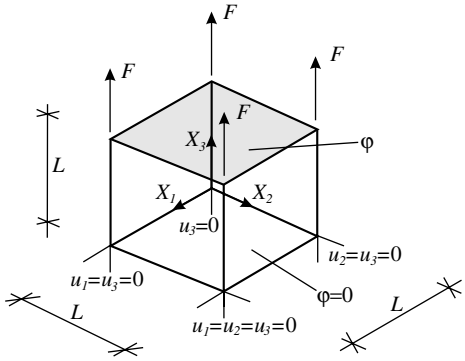

Fig. 6. Boundary and loading conditions of the piezoelectric specimen.

Table 1
Applied material parameters

PZT ceramic
$E_1 = E_2 = E_3 = 80 \times 10^6$ kN/m^2
$\nu_{12} = \nu_{13} = \nu_{23} = 0$
$G_{12} = G_{13} = G_{23} = 40 \times 10^6$ kN/m^2
$e_{13} = -12.0$ C/m^2, $e_{33} = 25.5802$ C/m^2, $e_{15} = -12.0$ C/m^2
$\epsilon = 15 \times 10^{-6}$ C^2/kN m^2
$E_s^i = 0.002$
$\vec{E}_s^i = 20 \times 10^3$ kV/m
$\vec{P}_c = 1.5 \times 10^{-2}$ C/m^2
$S_c = 50 \times 10^3$ GN/m^2
$\xi = 0.27$
$h = 1 \times 10^6$ kN/m^2, $m_t = 1$, $m_c = 1$
$k = \epsilon \cdot 0.999$, $a = 0.02/\text{arctanh}(1/b)$ C/m^2, $b = 1.00005$
$\zeta = 0.1 \times 10^6$ kN/m^2

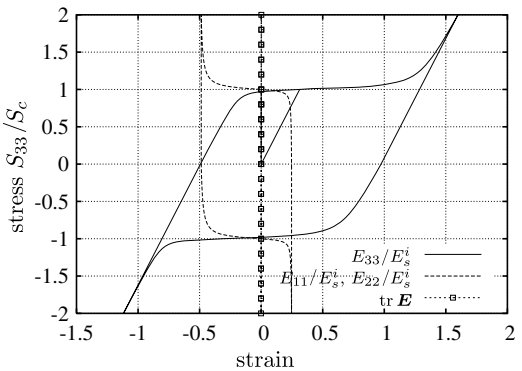

Fig. 7. Ferroelastic hysteresis.

large as the saturation strain. This effect coincides with experimental data and is discussed in Kamlah (2001) and Landis (2002). It is remarked that during the loading domain switching due to the stress application is observed but no polarization occurs. Furthermore the strains E_{11}, E_{22}, which are perpendicular to the loading direction, along with the trace of $\boldsymbol{E}$ are depicted in Fig. 7. It is observe that no volumetric change occurs during the polarization process only deviatoric deformations are obtained. The results confirm Eq. $(27)_1$ and are in accordance with experimental investigations.

For the second load case a zero stress state ($F = 0$) is assumed, instead an electric potential φ is applied to the free end. The value is increased up to $\varphi = 10$ kV then decreased to $\varphi = -10$ kV and again increased to $\varphi = 5$ kV. During the loading the electric field is increased up to 2×10^3 kV/m. When the coercive electric field is reached domain switching starts and it stops when the polarization is equal to the saturation value. This situation is illustrated with the dielectric hysteresis in Fig. 8. Due to the domain switching irreversible strains occur, which lead to the butterfly loop shown in Fig. 9. It is remarked that all quantities on the x- and y-axis are normalized by the coercive and saturation values. Accordingly correct results are obtained if the graphs intersect the x- and y-axis at $+1$ and -1, which is the case in Figs. 8 and 9. In addition the strains E_{11}, E_{22} perpendicular to the load direction are depicted in Fig. 9. It is observed that the trace of $\boldsymbol{E}$ is equal to zero. This confirms that no volumetric change during polarization arises.

The convergence rates of the proposed algorithms are discussed by analyzing the different residua for a typical load step. The load is increased from $\varphi = 10.1$ kV to $\varphi = 10.5$ kV and is marked with two dots in Figs. 8 and 9. For the global iteration the norm of the residuum vector $\boldsymbol{R}$ is listed in Table 2. A typical local iteration within this load step is analyzed in Table 2 on the right hand side. Here, the four residua equations (28) are shown. It is noted that for all residua a quadratic convergence is obtained.

At the polarized piezoceramic a compression load is applied to obtain mechanical depolarization. The polarized ceramic is characterized by an irreversible strain, which is equal the saturation strain, and an irreversible electric field, which is also equal to the saturation value. The compression load is increased from $F = 0$ kN up to $F = -30$ kN afterwards decreased to $F = 0$, where ϕ is assumed to be zero and therefore no electric field occurs. A typical mechanical depolarization curve is shown in Fig. 10. During the mechanical depolarization domain switching arises, which influences the dielectric displacement response. Furthermore irreversible strains may be obtained resulting from domain switching.

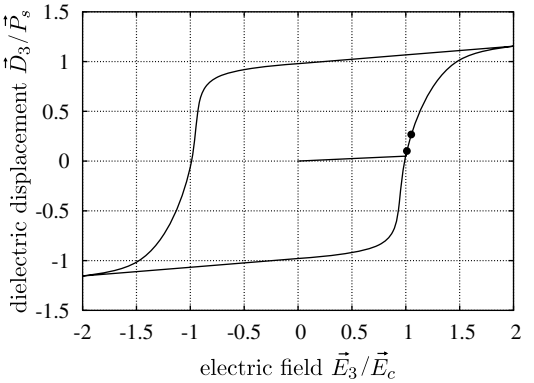

Fig. 8. Dielectric hysteresis.

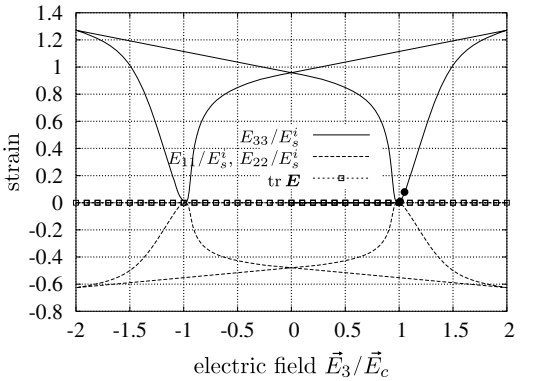

Fig. 9. Butterfly loop.

Table 2
The convergence behavior of the proposed algorithms

Iter	Global iteration	Local iteration			
	$\|\boldsymbol{R}\|$	$\|\boldsymbol{R}_a\|$	$\|\boldsymbol{R}_b\|$	R_c	R_d
1	2.0×10^{-01}	$0.1\times10^{+00}$	0.2×10^{-03}	0.1×10^{-02}	$0.1\times10^{+00}$
2	1.8×10^{-01}	0.2×10^{-01}	0.1×10^{-03}	0.3×10^{-03}	0.5×10^{-01}
3	1.2×10^{-02}	0.9×10^{-01}	0.8×10^{-04}	0.4×10^{-02}	0.1×10^{-01}
4	1.1×10^{-04}	0.3×10^{-01}	0.6×10^{-04}	0.2×10^{-02}	0.2×10^{-01}
5	9.1×10^{-09}	0.1×10^{-01}	0.3×10^{-04}	0.1×10^{-03}	0.1×10^{-01}
6	1.9×10^{-14}	0.2×10^{-02}	0.5×10^{-05}	0.1×10^{-03}	0.1×10^{-03}
7		0.1×10^{-04}	0.2×10^{-07}	0.1×10^{-06}	0.3×10^{-04}
8		0.1×10^{-07}	0.8×10^{-10}	0.1×10^{-08}	0.4×10^{-08}
9		0.5×10^{-14}	0.4×10^{-19}	0.6×10^{-16}	0.1×10^{-15}

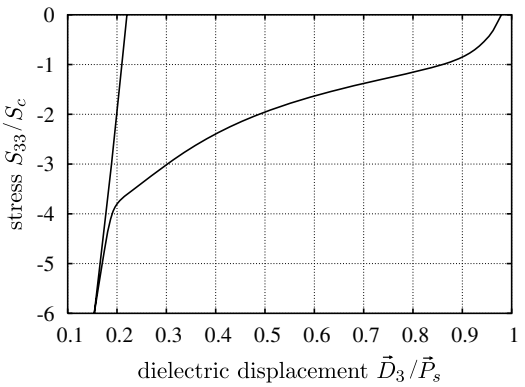

Fig. 10. Mechanical depolarization curve.

Experimental investigations, see e.g. Lynch (1996), lead exactly to the type of curves, which are presented in Figs. 7–10, which confirms that the proposed phenomenological model is able to capture the main characteristics of domain switching effect in piezoelectric ceramics.

6.2. Simulation of PLZT

The intention of this example is a comparison between the developed constitutive model with experimental data. In particular the electrical polarization and the mechanical depolarization of lead lanthanum zirconate titanate (PLZT) is simulated. The experimental data are presented in the work of Hwang et al. (1995). Considering the measured material data in Hwang et al. (1995) the coercive electric field $\vec{E}_c = 0.36\times10^6$ V/m, the coercive stress $S_c = 7\times10^6$ N/m^2, the saturation polarization $\vec{P}_s = 0.25$ C/m^2 and the saturation irreversible strain $E^i_s = 0.00144$ are given. With respect to the proposed material model the irreversible saturation strain and the coercive polarization are obtained as $\vec{E}^i_s = \vec{P}_s/\epsilon$ and $\vec{P}_c = \vec{E}_s\epsilon$, where ϵ denotes the electric permittivity. For the one-dimensional model of Hwang et al. the Young's modulus is given as $E_3 = 86\times10^9$ N/m^2. Due to the fact that for the introduced three-dimensional constitutive model much more parameters are necessary, some of these are assumed and summarized in Table 3. The notation of the material tensors in matrix form is provided in Appendix A.

The specimen of cubic form has an edge length of $L = 10$ mm. It is subjected to an electric field for polarization and a stress for the mechanical depolarization process. According to the experimental setup, which is explained in detail in Hwang et al. (1995), the assumed boundary conditions for the calculation are shown in Fig. 6.

For the first load case the sample is subjected to an electric field; therefore the electric potential of the upper surface is increased, whereas the lower surface is grounded. With respect to Hwang et al. the voltage of 8 kV is

Table 3
Applied material parameters for lead lanthanum zirconate titanate (PLZT)

PLZT ceramic
$E_1 = E_2 = E_3 = 68$ GN/m^2
$\nu_{12} = \nu_{13} = \nu_{23} = 0.35$
$G_{12} = G_{13} = G_{23} = 25.186$ GN/m^2
$e_{13} = -14.96$ C/m^2, $e_{33} = 50.116$ C/m^2, $e_{15} = 38.148$ C/m^2
$\epsilon = 1.125$ C^2/GN m^2
$E_s^i = 0.00144$
$\vec{E}_s^i = 0.22222$ GV/m
$\vec{P}_c = 0.405 \times 10^{-3}$ C/m^2
$S_c = 7 \times 10^{-3}$ GN/m^2
$\xi = 0.032$
$h = 1.0$ GN/m^2, $m_t = 1$, $m_c = 1.2$
$k = \epsilon \cdot 0.9999$, $a = 0.0003/\text{arctanh}(1/b)$ C/m^2, $b = 1.001$
$\zeta = 0.01$ GN/m^2

applied in a triangle wave with an operating frequency of 0.02 Hz. Due to the small frequency it is assumed that no time effects occur, in other words a quasi static loading and unloading is applied. The resulting dielectric hysteresis and butterfly loops at zero stress state are shown in Figs. 11 and 12.

In the second load case the fully polarized ceramic is subjected to a compression stress. The example is initially at zero stress with the maximum remanent strain and the maximum remanent polarization. The load F is

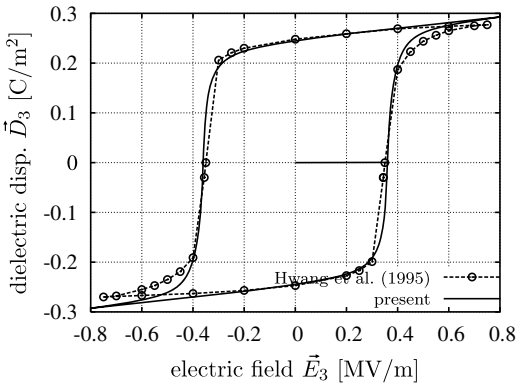

Fig. 11. Comparison of the simulation and the measured experimental data in Hwang et al. (1995) of a PLZT sample; dielectric hysteresis.

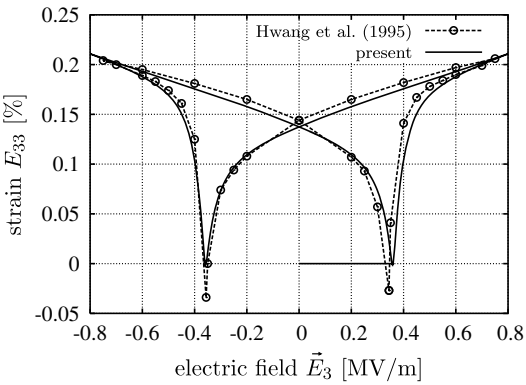

Fig. 12. Comparison of the simulation and the measured experimental data in Hwang et al. (1995) of a PLZT sample; butterfly loop.

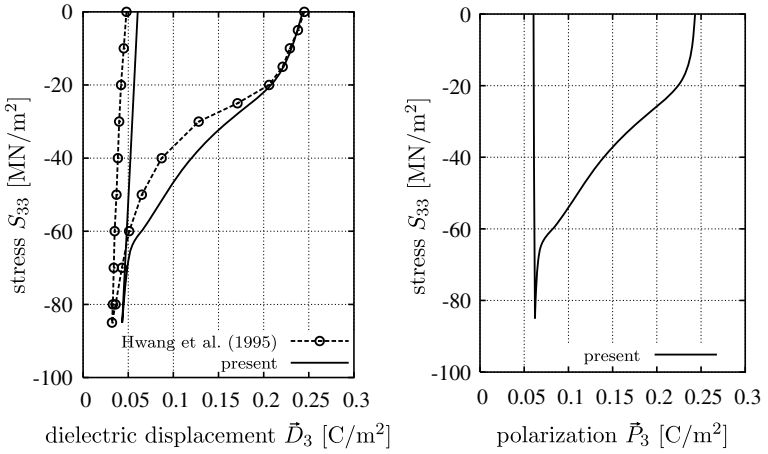

Fig. 13. Comparison of the simulation and the measured experimental data in Hwang et al. (1995) of a PLZT sample; left: compression stress vs. dielectric displacement; right: compression stress vs. polarization.

increased form $F = 0$ N up to $F = -2125$ N, which leads to a compression stress $S_{33} = -85 \times 10^6$ N. Afterwards the sample is unloaded again. The resulting depolarization curves are depicted in Fig. 13.

The polarization which is shown in Fig. 13 on the left hand side is calculated form the irreversible electric field as $\vec{P}_3 = -\epsilon \vec{E}_3^{\,i}$. It is obtained that after polarization the resulting $\vec{P}_3$ is close to zero.

Figs. 11–13 show a good agreement of the simulation and the measured experimental data, which confirms that the proposed constitutive model is able to approximate the realistic material behavior.

6.3. Non-remanent straining ferroelectrics

This example is concerned with the simulation of non-remanent straining ferroelectric ceramics. It demonstrates the manifold applicability of the proposed formulation. Non-remanent straining ferroelectrics were experimentally observed by e.g. Schneider and Heyer (1999). A constitutive model considering this effect was suggested by Landis (2002). In contrast to the present formulation Landis employed the irreversible strain and the polarization vector as internal variables.

For the simulation of the dielectric hysteresis and the butterfly loops the system illustrated in Fig. 6 with $L = 10$ mm is used. The material data is summarized in Table 4. It is noted that the influence of the third

Table 4
Applied material parameters

PLZT ceramic
$E_1 = E_2 = E_3 = 80 \times 10^6$ kN/m^2
$\nu_{12} = \nu_{13} = \nu_{23} = 0$
$G_{12} = G_{13} = G_{23} = 40 \times 10^6$ kN/m^2
$e_{13} = -4.8$ C/m^2, $e_{33} = 10.232$ C/m^2, $e_{15} = -4.8$ C/m^2
$\epsilon = 15 \times 10^{-6}$ C^2/kN m^2
$E_s^i = 0.002$
$\vec{E}_s^{\,i} = 20 \times 10^3$ kV/m
$\vec{P}_c = 1.5 \times 10^{-2}$ C/m^{-2}
$S_c = 50 \times 10^3$ GN/m^2
$\xi = 0.25$
$h = 1 \times 10^6$ kN/m^2, $m_t = 1$, $m_c = 1$
$k = \epsilon \cdot 0.999$, $a = 0.04/\text{arctanh}(1/b)$ C/m^2, $b = 1.1$
$\zeta = 0.1$ kN/m^2

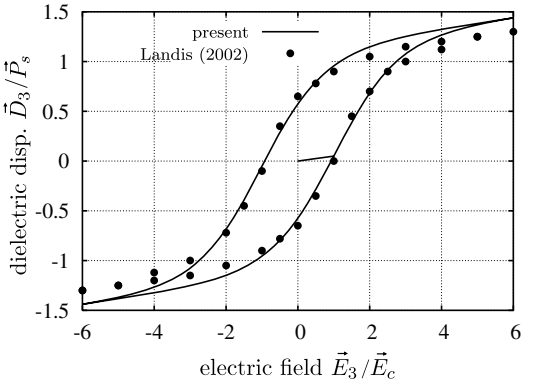

Fig. 14. Constitutive response of non-remanent straining ferroelectrics; dielectric hysteresis.

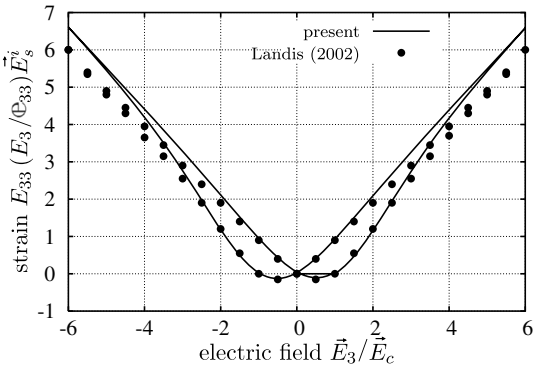

Fig. 15. Constitutive response of non-remanent straining ferroelectrics; butterfly loop.

hardening function is significantly reduced with $\zeta = 0.1\ \mathrm{kN/m^2}$, which means that an irreversible electric field has no influence on the irreversible strain.

The system is loaded by increasing the electric potential up to $\varphi = 60$ kV afterwards decreasing the load to $\varphi = -60$ kV and finally the electric potential is increased again up to $\varphi = 10$ kV. The resulting dielectric displacements and the irreversible strains are depicted in Figs. 14 and 15 and a comparison to the normalized values obtained by Landis (2002) is provided. A good agreement of both models is observed. It is noted that, when the electric field after polarization is decreased to zero no irreversible strain remains.

6.4. Cantilever beam problem

In this example the non-linear effects which arise due to mechanical depolarization are illustrated by applying a tip force to a polarized cantilever beam. The cantilever beam is modeled with $20 \times 16 \times 2$ finite brick elements, see Fig. 16. The material data is the same as for the first example and is summarized in Table 1.

The system is loaded by applying an electric potential φ to the tip of the cantilever, which is increased up to $\varphi = -2 \times 10^{-5}$ GV and afterwards decreased to $\varphi = 0$. As result one gets a polarized ferroelectric ceramic. It is characterized by the saturation strain $E_{\mathrm{s}}^{\mathrm{i}}$ and by an remanent saturation polarization $\vec{P}_{\mathrm{s}}$ or in other words by the irreversible saturation electric field $\vec{E}_{\mathrm{s}}^{\mathrm{i}}$. The polarized ceramic is considered as an initial state for the second load case, in which the transverse force is subjected to the tip of the cantilever. It is increased up to $F = 122.9$ N. The load deflection curve is depicted in Fig. 17. The bending of the beam which is caused by the transverse force leads to a compression stress. If the compression stress reaches the coercive value, domain switching occurs. The mechanical depolarization is responsible for the non-linear behavior of the load

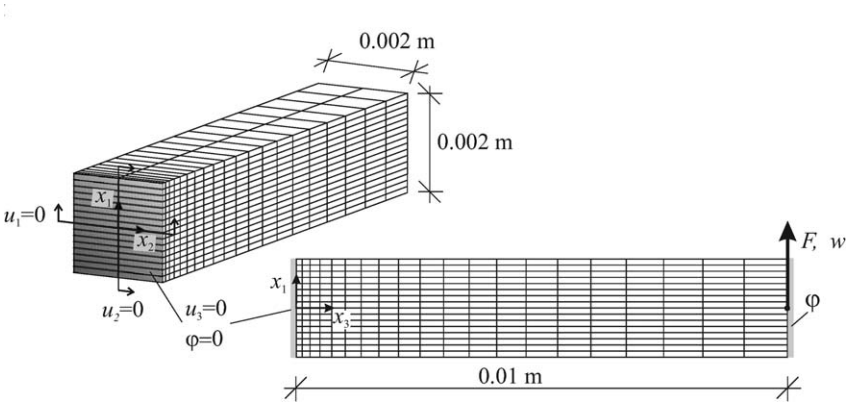

Fig. 16. Cantilever beam: system, boundary conditions and geometry data.

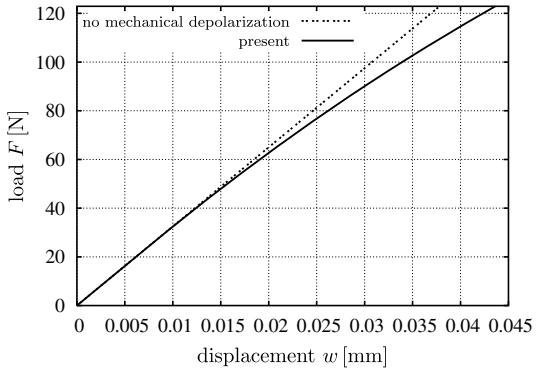

Fig. 17. The force F vs. the deflection w of the cantilever tip.

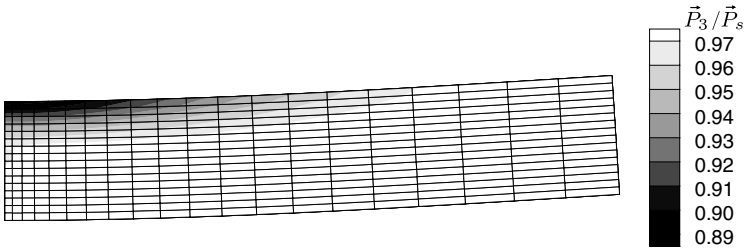

Fig. 18. The deformed cantilever amplified by factor 10 with a plot of the normalized polarization.

deflection curve. For comparison the behavior of a model for which no mechanical depolarization is allowed is given in Fig. 17.

The deformed mesh with a plot of the normalized polarization vector in x_3-direction $\vec{P}_3/\vec{P}_s$ is shown in Fig. 18. The zones in which domain switching occurs are clearly visible.

7. Concluding remarks

In this paper a thermodynamic consistent phenomenological model for ferroelastic and ferroelectric switching is presented. The main idea is to introduce an irreversible electric field, which serves beside the irreversible strain as internal variables. The evolution equations are derived by the principle of maximum dissipation and

are integrated with implicit time integration algorithm. The model is in full accordance with the numerical solution of the irreversible boundary value problem by the finite element method employing displacements and electric potential as nodal degrees of freedom. The constitutive relationship is not simplified by a one-to-one relationship between the polarization and the irreversible strain. Instead an additive split of the irreversible strains is suggest. A special hardening function is introduced to accomplish enough space in terms of irreversible strain for the ferroelectric switching process. A consistent finite element implementation is presented. The examples demonstrate the superior numerical behavior of the formulation and show that the model accounts for the ferroelastic and ferroelectric hysteresis effects as well as for the mechanical depolarization.

Acknowledgement

The author acknowledges Professor Dr.-Ing. Werner Wagner, Institut für Baustatik, Universität Karlsruhe, for his discussion and support.

Appendix A. Linear material properties

For the sake of simplicity we assume that all material properties referring to a Cartesian co-ordinate system. The stress tensor and the strain tensor are represented in vector notation as

$$\begin{aligned} \boldsymbol{S} &= [S_{11}, S_{22}, S_{33}, S_{12}, S_{13}, S_{23}]^{\mathrm{T}}, \\ \boldsymbol{E} &= [E_{11}, E_{22}, E_{33}, 2E_{12}, 2E_{13}, 2E_{23}]^{\mathrm{T}}. \end{aligned} \tag{A.1}$$

The elasticity tensor in matrix representation is given by

$$\mathbb{C}^{-1} = \begin{bmatrix} \frac{1}{E_1} & -\frac{\nu_{12}}{E_2} & -\frac{\nu_{13}}{E_3} & 0 & 0 & 0 \\ -\frac{\nu_{12}}{E_2} & \frac{1}{E_2} & -\frac{\nu_{23}}{E_3} & 0 & 0 & 0 \\ -\frac{\nu_{13}}{E_3} & -\frac{\nu_{23}}{E_3} & \frac{1}{E_3} & 0 & 0 & 0 \\ 0 & 0 & 0 & \frac{1}{G_{12}} & 0 & 0 \\ 0 & 0 & 0 & 0 & \frac{1}{G_{13}} & 0 \\ 0 & 0 & 0 & 0 & 0 & \frac{1}{G_{23}} \end{bmatrix}. \tag{A.2}$$

Here, the Young's moduli E_1, E_2, E_3, the Poisson's ratios ν_{12}, ν_{13}, ν_{23} and the shear moduli G_{12}, G_{13}, G_{23} are independent material parameters. The piezoelectric matrix $\mathbb{e}$ and the permittivity matrix $\boldsymbol{\epsilon}$ read

$$\mathbb{e} = \begin{bmatrix} 0 & 0 & 0 & 0 & \mathbb{e}_{15} & 0 \\ 0 & 0 & 0 & 0 & 0 & \mathbb{e}_{15} \\ \mathbb{e}_{13} & \mathbb{e}_{13} & \mathbb{e}_{33} & 0 & 0 & 0 \end{bmatrix}, \qquad \boldsymbol{\epsilon} = \epsilon \begin{bmatrix} 1 & 0 & 0 \\ 0 & 1 & 0 \\ 0 & 0 & 1 \end{bmatrix}, \tag{A.3}$$

where $\mathbb{e}_{13}$, $\mathbb{e}_{33}$, $\mathbb{e}_{15}$ and ϵ represent independent material parameters. All parameters are given within the numerical examples in Section 6.

Appendix B. Derivatives for local Newton-iteration

For the local iteration scheme given in Section 3.1 the following derivatives are necessary to evaluate Eqs. (29):

$$
\begin{aligned}
\frac{\partial \boldsymbol{R}_a}{\partial \boldsymbol{E}^{\mathrm{Pi}}} &= \mathbb{I} + \gamma \frac{3}{S_{\mathrm{c}}^2}\mathbb{P} : \left(\mathbb{C} + \frac{\partial\partial \bar{\psi}}{\partial \boldsymbol{E}^{\mathrm{i}} \partial \boldsymbol{E}^{\mathrm{Pi}}} \right), \\
\frac{\partial \boldsymbol{R}_a}{\partial \boldsymbol{E}^{\mathrm{Si}}} &= \gamma \frac{3}{S_{\mathrm{c}}^2}\mathbb{P} : \left(\mathbb{C} + \frac{\partial\partial \bar{\psi}}{\partial \boldsymbol{E}^{\mathrm{i}} \partial \boldsymbol{E}^{\mathrm{Si}}} \right), \\
\frac{\partial \boldsymbol{R}_a}{\partial \beta} &= -\gamma \frac{3}{S_{\mathrm{c}}^2}\mathbb{P} : \left(\mathbb{e}^{\mathrm{T}} \vec{\boldsymbol{E}} \frac{1}{\vec{E}_{\mathrm{s}}^{\mathrm{i}}} + \frac{\partial\partial \bar{\psi}}{\partial \boldsymbol{E}^{\mathrm{i}} \partial \vec{\boldsymbol{E}}^{\mathrm{i}}} e_{\mathrm{p}} \right), \\
\frac{\partial \boldsymbol{R}_a}{\partial \gamma} &= -\frac{3}{S_{\mathrm{c}}^2}\mathbb{P} : \widehat{\boldsymbol{S}},
\end{aligned}
\tag{B.1}
$$

$$
\begin{aligned}
\frac{\partial \boldsymbol{R}_b}{\partial \boldsymbol{E}^{\mathrm{Pi}}} &= \gamma\xi \frac{1}{S_{\mathrm{c}}^2 \vec{P}_{\mathrm{s}}^2} (\widehat{\boldsymbol{P}} \cdot \boldsymbol{e}_{\mathrm{p}})^2 \frac{\partial\partial f}{\partial \boldsymbol{S} \partial \boldsymbol{S}} : \mathbb{C}, \\
\frac{\partial \boldsymbol{R}_b}{\partial \boldsymbol{E}^{\mathrm{Si}}} &= \mathbb{I} + \gamma\xi \frac{1}{S_{\mathrm{c}}^2 \vec{P}_{\mathrm{s}}^2} (\widehat{\boldsymbol{P}} \cdot \boldsymbol{e}_{\mathrm{p}})^2 \frac{\partial\partial f}{\partial \boldsymbol{S} \partial \boldsymbol{S}} : \mathbb{C}, \\
\frac{\partial \boldsymbol{R}_b}{\partial \beta} &= -\gamma\xi \frac{1}{S_{\mathrm{c}}^2 \vec{P}_{\mathrm{s}}^2} \left(\frac{1}{\vec{E}_{\mathrm{s}}^{\mathrm{i}}} (\widehat{\boldsymbol{P}} \cdot \boldsymbol{e}_{\mathrm{p}})^2 \frac{\partial\partial f}{\partial \boldsymbol{S} \partial \boldsymbol{S}} : \mathbb{e}^{\mathrm{T}} \vec{\boldsymbol{E}} + 2 (\widehat{\boldsymbol{P}} \cdot \boldsymbol{e}_{\mathrm{p}}) (\boldsymbol{\epsilon} : \boldsymbol{M}) \frac{\partial f}{\partial \boldsymbol{S}} \right), \\
\frac{\partial \boldsymbol{R}_b}{\partial \gamma} &= -\xi \frac{1}{S_{\mathrm{c}}^2 \vec{P}_{\mathrm{s}}^2} (\widehat{\boldsymbol{P}} \cdot \boldsymbol{e}_{\mathrm{p}})^2 \frac{\partial f}{\partial \boldsymbol{S}},
\end{aligned}
\tag{B.2}
$$

$$
\begin{aligned}
\frac{\partial R_{\mathrm{c}}}{\partial \boldsymbol{E}^{\mathrm{Pi}}} &= \gamma \frac{2}{\vec{P}_{\mathrm{c}}^2} \left(\boldsymbol{e}_{\mathrm{p}} \cdot \frac{\partial\partial \bar{\psi}}{\partial \vec{\boldsymbol{E}}^{\mathrm{i}} \partial \boldsymbol{E}^{\mathrm{Pi}}} - \mathbb{e}^{\mathrm{T}} \vec{\boldsymbol{E}} \frac{1}{\vec{E}_{\mathrm{s}}^{\mathrm{i}}} \right) + \gamma\xi \frac{2}{S_{\mathrm{c}}^2 \vec{P}_{\mathrm{s}}^2} (\vec{\boldsymbol{P}} \cdot \boldsymbol{e}_{\mathrm{p}}) \frac{\partial f}{\partial \boldsymbol{S}} : \mathbb{C}, \\
\frac{\partial R_{\mathrm{c}}}{\partial \boldsymbol{E}^{\mathrm{Si}}} &= \gamma \frac{2}{\vec{P}_{\mathrm{c}}^2} \left(\boldsymbol{e}_{\mathrm{p}} \cdot \frac{\partial\partial \bar{\psi}}{\partial \vec{\boldsymbol{E}}^{\mathrm{i}} \partial \boldsymbol{E}^{\mathrm{Si}}} - \mathbb{e}^{\mathrm{T}} \vec{\boldsymbol{E}} \frac{1}{\vec{E}_{\mathrm{s}}^{\mathrm{i}}} \right) + \gamma\xi \frac{2}{S_{\mathrm{c}}^2 \vec{P}_{\mathrm{s}}^2} (\vec{\boldsymbol{P}} \cdot \boldsymbol{e}_{\mathrm{p}}) 2 \frac{\partial f}{\partial \boldsymbol{S}} : \mathbb{C},
\end{aligned}
\tag{B.3}
$$

$$
\begin{aligned}
\frac{\partial R_{\mathrm{c}}}{\partial \beta} &= 1 + \gamma \frac{2}{\vec{P}_{\mathrm{c}}^2} \boldsymbol{M} : \left(\frac{\partial\partial \bar{\psi}}{\partial \vec{\boldsymbol{E}}^{\mathrm{i}} \partial \boldsymbol{E}^{\mathrm{i}}} - \boldsymbol{\epsilon} \right) - \gamma\xi \frac{2}{S_{\mathrm{c}}^2 \vec{P}_{\mathrm{s}}^2} \left(\frac{1}{\vec{E}_{\mathrm{s}}^{\mathrm{i}}} (\widehat{\boldsymbol{P}} \cdot \boldsymbol{e}_{\mathrm{p}}) \frac{\partial f}{\partial \boldsymbol{S}} : \mathbb{e}^{\mathrm{T}} \vec{\boldsymbol{E}} + f (\boldsymbol{M} : \boldsymbol{\epsilon}) \right), \\
\frac{\partial R_{\mathrm{c}}}{\partial \gamma} &= -\frac{2}{\vec{P}_{\mathrm{c}}^2} (\widehat{\boldsymbol{D}} \cdot \boldsymbol{e}_{\mathrm{p}}) - \xi \frac{2}{S_{\mathrm{c}}^2 \vec{P}_{\mathrm{s}}^2} f (\widehat{\boldsymbol{P}} \cdot \boldsymbol{e}_{\mathrm{p}})
\end{aligned}
$$

$$
\begin{aligned}
\frac{\partial \boldsymbol{R}_d}{\partial \boldsymbol{E}^{\mathrm{Pi}}} &= -\frac{3}{S_{\mathrm{c}}^2} \boldsymbol{S} : \mathbb{P} : \left(\mathbb{C} + \frac{\partial\partial \bar{\psi}}{\partial \boldsymbol{E}^{\mathrm{i}} \partial \boldsymbol{E}^{\mathrm{Pi}}} \right) + \frac{2}{\vec{P}_{\mathrm{c}}^2} (\widehat{\boldsymbol{D}} \cdot \boldsymbol{e}_{\mathrm{p}}) \left(\frac{1}{\vec{E}_{\mathrm{s}}^{\mathrm{i}}} \mathbb{e}^{\mathrm{T}} \vec{\boldsymbol{E}} - \frac{\partial\partial \bar{\psi}}{\partial \boldsymbol{E}^{\mathrm{i}} \partial \boldsymbol{E}^{\mathrm{Pi}}} \right) - \xi \frac{1}{S_{\mathrm{c}}^2 \vec{P}_{\mathrm{s}}^2} (\widehat{\boldsymbol{P}} \cdot \boldsymbol{e}_{\mathrm{p}})^2 \frac{\partial f}{\partial \boldsymbol{S}} : \mathbb{C}, \\
\frac{\partial R_d}{\partial \boldsymbol{E}^{\mathrm{Si}}} &= -\frac{3}{S_{\mathrm{c}}^2} \boldsymbol{S} : \mathbb{P} : \left(\mathbb{C} + \frac{\partial\partial \bar{\psi}}{\partial \boldsymbol{E}^{\mathrm{i}} \partial \boldsymbol{E}^{\mathrm{Si}}} \right) + \frac{2}{\vec{P}^2} (\widehat{\boldsymbol{D}} \cdot \boldsymbol{e}_{\mathrm{p}}) \left(\frac{1}{\vec{E}_{\mathrm{s}}^{\mathrm{i}}} \mathbb{e}^{\mathrm{T}} \vec{\boldsymbol{E}} - \frac{\partial\partial \bar{\psi}}{\partial \vec{\boldsymbol{E}}^{\mathrm{i}} \partial \boldsymbol{E}^{\mathrm{Si}}} \right) - \xi \frac{1}{S_{\mathrm{c}}^2 \vec{P}_{\mathrm{s}}^2} (\widehat{\boldsymbol{P}} \cdot \boldsymbol{e}_{\mathrm{p}})^2 \frac{\partial f}{\partial \boldsymbol{S}} : \mathbb{C},
\end{aligned}
\tag{B.4}
$$

$$
\begin{aligned}
\frac{\partial R_d}{\partial \beta} &= \frac{3}{S_{\mathrm{c}}^2} \boldsymbol{S} : \mathbb{P} : \left(\mathbb{e}^{\mathrm{T}} \vec{\boldsymbol{E}} \frac{1}{\vec{E}_{\mathrm{s}}^{\mathrm{i}}} - \frac{\partial\partial \bar{\psi}}{\partial \boldsymbol{E}^{\mathrm{i}} \partial \vec{\boldsymbol{E}}^{\mathrm{i}}} e_{\mathrm{p}} \right) + \frac{2}{\vec{P}_{\mathrm{c}}^2} (\widehat{\boldsymbol{D}} \cdot \boldsymbol{e}_{\mathrm{p}}) \boldsymbol{M} : \left(\boldsymbol{\epsilon} - \frac{\partial\partial \bar{\psi}}{\partial \boldsymbol{E}^{\mathrm{i}} \partial \vec{\boldsymbol{E}}^{\mathrm{i}}} \right), \\
&\quad + \xi \frac{1}{S_{\mathrm{c}}^2 \vec{P}_{\mathrm{s}}^2} \left(\frac{1}{\vec{E}_{\mathrm{s}}^{\mathrm{i}}} (\widehat{\boldsymbol{P}} \cdot \boldsymbol{e}_{\mathrm{p}})^2 \frac{\partial f}{\partial \boldsymbol{S}} : \mathbb{e}^{\mathrm{T}} \vec{\boldsymbol{E}} + 2 f (\widehat{\boldsymbol{P}} \cdot \boldsymbol{e}_{\mathrm{p}}) (\boldsymbol{M} : \boldsymbol{\epsilon}) \right)
\end{aligned}
\tag{B.5}
$$

$$
\frac{\partial R_d}{\partial \gamma} = 0.
$$

In the case $\boldsymbol{S} : \mathbb{P} : \boldsymbol{M} \geqslant 0$ the derivative of $\frac{\partial\partial f}{\partial \boldsymbol{S} \partial \boldsymbol{S}} = 0$ otherwise $\frac{\partial\partial f}{\partial \boldsymbol{S} \partial \boldsymbol{S}} = \frac{9}{2} (\mathbb{P} : \boldsymbol{M} \otimes \boldsymbol{M} : \mathbb{P})$. The derivative $\frac{\partial f}{\partial \boldsymbol{S}}$ is given in Eq. (22).

References

Bassiouny, E., Maugin, G., 1989a. Thermodynamical formulation for coupled electromechanical hysteresis effects—III. parameter identification. International Journal of Engineering Science 27 (8), 975–987.

Bassiouny, E., Maugin, G., 1989b. Thermodynamical formulation for coupled electromechanical hysteresis effects—IV. combined electromechanical loading. International Journal of Engineering Science 27 (8), 989–1000.

Bassiouny, E., Ghaleb, A., Maugin, G., 1988a. Thermodynamical formulation for coupled electromechanical hysteresis effects—I. basic equations. International Journal of Engineering Science 26 (12), 1279–1295.

Bassiouny, E., Ghaleb, A., Maugin, G., 1988b. Thermodynamical formulation for coupled electromechanical hysteresis effects—II. poling of ceramics. International Journal of Engineering Science 26 (12), 1297–1306.

Benjeddou, A., 2000. Advances in piezoelectric finite element modeling of adaptive structural elements: a survey. Computers and Structures 76, 347–363.

Butz, A., Klinkel, S., Wagner, W., 2005. A nonlinear piezo electric 3d-beam finite element formulation. In: Bathe, K. (Ed.), Proceedings Third MIT Conference on Computational Fluid and Solid Mechanics. Massachusetts Institute of Technology, Cambridge, pp. 291–296.

Chadwick, P., Ogden, R., 1971. On the definition of elastic material. Archive for Rational Mechanics and Analysis 44, 41–53.

Chen, P., 1980. Three dimensional dynamic electromechanical constitutive relations for ferroelectric materials. International Journal of Solids and Structures 16, 1059–1067.

Chen, W., Lynch, C., 1998. A micro-electro-mechanical model for polarization switching of ferrroelectric materials. Acta Metallurgica 46 (15), 5303–5311.

Chen, P., Montgomery, S., 1980. A macroscopic theory for the existence of the hysteresis and butterfly loops in ferroelectricity. Ferroelectrics 23, 199–208.

Chen, P., Tucker, T., 1981. One dimensional polar mechanical and dielectric responses of the ferroelectric ceramic PZT 65/35 due to domain switching. International Journal of Engineering Science 19, 147–158.

Cocks, A., McMeeking, R., 1999. A phenomenological constitutive law for the behaviour of ferroelectric ceramics. Ferroelectrics 228, 219–228.

Elhadrouz, M., Zineb, T., Patoor, E., 2004. Phenomenological modelling of the non-linear behavior of ferroelectric materials. In: Lexcellent, C. Patoor, E. (Eds.), Journal de Physique IV—Proceedings 7th European Mechanics of Materials Conference on Adaptive Systems and Materials: Constitutive Materials and Hybrid Structures. vol. 115. Frjus, France, pp. 67–72.

Elhadrouz, M., Zineb, T., Patoor, E., 2005. Constitutive law for ferroelastic and ferroelectric piezoceramics. Journal of Intelligent Material Systems and Structures 16, 221–263.

Eringen, A., Maugin, G., 1990. Electrodynamics of Continua. Foundations and Solid Media. vol. I. Springer.

Fett, T., Müller, S., Munz, D., Thun, G., 1998. Nonsymmetry in the deformation behavior of pzt. Journal of Materials Science Letters 17, 261–265.

Gaudenzi, P., Bathe, K., 1995. An iterative finite element procedure for the analysis of piezoelektric continua. Journal of Intelligent Material Systems and Structures 6, 266–273.

Ghandi, K., Hagood, N., 1997. A hybrid finite element model for phase transition in nonlinear electro-mechanically coupled material. In: Varadan, V., Chandra, J. (Eds.), Proceedings of SPIE: Smart Structures and Materials. vol. 3039. Washington, pp. 97–112.

Huber, J., Fleck, N., 2001. Multi-axial electrical switching of a ferroelectric: theory versus experiment. Journal of the Mechanics and Physics of Solids 49, 785–811.

Huber, J., Fleck, N., Landis, C., McMeeking, R., 1999. A constitutive model for ferroelectric polycrystals. Journal of the Mechanics and Physics of Solids 47, 1663–1697.

Hwang, S., McMeeking, R., 1999. A finite element model of ferroelastic polycrystals. International Journal of Solids and Structures 36, 1541–1556.

Hwang, S., Lynch, C., McMeeking, R., 1995. Ferroelectric/ferroelastic interactions and a polarization switching model. Acta Metallurgica et Materialia 43, 2073–2084.

Hwang, S., Huber, J., McMeeking, R., Fleck, N., 1998. The simulation of switching in poly crystalline ferroelectric ceramics. Journal of Applied Physics 84 (3), 1530–1540.

Ikeda, T., 1990. Fundamentals of Piezoelectricity. ORD University Press, Oxford.

Jendritza, D., 2005. Technischer Einsatz neuer Aktoren, third ed. Kontakt and Studium, vol. 484 Expert Verlag.

Kamlah, M., 2001. Ferroelectric and ferroelastic piezoceramics—modeling of electromechanical hysteresis phenomena. Continuum Mechanics and Thermodynamics 13, 219–268.

Kamlah, M., Böhle, U., 2001. Finite element analysis of piezoceramic components taking into account ferroelectric hysteresis behavior. International Journal of Solids and Structures 38, 605–633.

Kamlah, M., Tsakmakis, C., 1999. Phenomenological modelling of the nonlinear electro-mechanical coupling in ferroelectrics. International Journal of Solids and Structures 36, 669–695.

Klinkel, S., Wagner, W., 2006. A geometrically non-linear piezoelectric solid shell element based on a mixed multi-field variational formulation. International Journal for Numerical Methods in Engineering 65 (3), 349–382.

Landis, C., 2002. Fully coupled multi-axial, symmetric constitutive laws for poly crystalline ferroelectric ceramics. Journal of the Mechanics and Physics of Solids 50, 127–152.

Lynch, C., 1996. The effect of uniaxial stress on the electro-mechanical response of 8/65/35 plzt. Acta Materialia 44, 4137–4148.

Maluf, N., Williams, K., 2004. An Introduction to Microelectromechanical Systems Engineering, Microelectromechanical Systems, second ed. Artech House, Boston/London.

Maugin, C., 1988. Continuum mechanics of electromagnetic solids. In: Achen-bach, J., Budiansky, B., Koiter, W., Lauwerier, H.A., Van Wijngaarden, L. (Eds.), Applied Mathematics and Mechanics. vol. 33. North-Holland Series, pp. 1–598.

McMeeking, R., Landis, C., 2002. A phenomenological multi-axial constitutive switching in polycrystalline ferroelectric ceramics. International Journal of Engineering Science 40, 1553–1577.

Moulson, A., Herbert, J., 2003. Electroceramics: Materials, Properties, Applications. second ed. Wiley.

Niezrecki, C., Brei, D., Balakrishnan, S., Moskalik, A., 2001. Piezoelectric actuation: state of the art. The Shock and Vibration Digest 33 (4), 269–280.

Pasco, Y., Berry, A., 2004. A hybrid analytical/numerical model of piezoelectric stack actuators using a macroscopic nonlinear theory of ferroelectricity and a Preisach model of hysteresis. Journal of Intelligent Material Systems and Structures 15, 375–386.

Preisach, E., 1935. Über die magnetische Nachwirkung. Zeitschrift für Physik 94, 277–302.

Schneider, G., Heyer, V., 1999. Influence of the electric field on Vickers identation crack growth in $BaTiO_3$. Journal of the European Ceramic Society 19, 1299–1306.

Schröder, J., Gross, D., 2004. Invariant formulation of the electromechanical enthalpy function of transversely isotropic piezoelectric materials. Archive of Applied Mechanics 73, 533–552.

Schröder, J., Romanowski, H., 2004. A simple coordinate invariant thermodynamic consistent model for nonlinear electro-mechanical coupled ferroelectrica. European Congress on Computational Methods in Applied Sciences and Engineering.

Schröder, J., Romanowski, H., 2005. A thermodynamically consistent mesoscopic model for transversely isotropic ferroelectric ceramics in a coordinate-invariant setting. Archive of Applied Mechanics 74, 863–877.

Simkovics, R., Landes, H., Kaltenbacher, M., Hoffelner, J., Lerch, R., 2000. Finite element analysis of hysteresis effects in piezoelectric transducers. In: Varadan, V. (Ed.), Proceedings of SPIE: Smart Structures and Materials. vol. 3984. Newport Beach, pp. 33–44.

Simo, J., 1998. Numerical analysis of classical plasticity. In: Ciarlet, P., Lions, J. (Eds.), Handbook of Numerical Analysis. North-Holland, pp. 183–499.

Simo, J., Hughes, T., 1998. Computational Inelasticity. Mechanics and Materials. vol. 7. Springer-Verlag, New York, Interdisciplinary Applied Mathematics.

Tani, J., Takagi, T., Qiu, J., 1998. Intelligent material systems: application of functional materials. Applied Mechanics Reviews 51 (8), 505–521.

Voigt, W., 1928. Lehrbuch der Kristallphysik, Nachdruck der 1. Auflage Edition. Teubner-Verlag, Leipzig/Berlin.

Wriggers, P., 2001. Nichtlineare Finite-Element-Methoden. Springer.

Yu, Y., Naganathan, N., Dukkipati, R., 2002. Preisach modeling of hysteresis for piezoceramic actuator system. Mechanism and Machine 37, 49–59.

Zeng, W., Manzari, M., Lee, J., Shen, Y., 2003. Fully coupled non-linear analysis of piezoelectric solids involving domain switching. International Journal for Numerical Methods in Engineering 56, 13–34.